Revisiting moment-closure methods with heterogeneous multiscale population models

Davin Lunz, Joseph Frédéric Bonnans, Jakob Ruess

To cite this version:

Davin Lunz, Joseph Frédéric Bonnans, Jakob Ruess. Revisiting moment-closure methods with heterogeneous multiscale population models. Mathematical Biosciences, 2022, 350, pp.108866. 10.1016/j.mbs.2022.108866 . hal-03479587v2

HAL Id: hal-03479587
https://inria.hal.science/hal-03479587v2

Submitted on 27 Jun 2022

Revisiting moment-closure methods with heterogeneous multiscale population models

Davin Lunz*[1,2], J. Frédéric Bonnans[3], and Jakob Ruess[1,2]

[1]Inria Paris, 2 rue Simone Iff, 75012 Paris, France
[2]Institut Pasteur, 28 rue du Docteur Roux, 75015 Paris, France
[3]Université Paris-Saclay, CNRS, CentraleSupélec, Inria, Laboratory of signals and systems,
91190, Gif-sur-Yvette, France

Abstract

Stochastic chemical kinetics at the single-cell level give rise to heterogeneous populations of cells even when all individuals are genetically identical. This heterogeneity can lead to nonuniform behaviour within populations, including different growth characteristics, cell-fate dynamics, and response to stimuli. Ultimately, these diverse behaviours lead to intricate population dynamics that are inherently multiscale: the population composition evolves based on population-level processes that interact with stochastically distributed single-cell states. Therefore, descriptions that account for this heterogeneity are essential to accurately model and control chemical processes. However, for real-world systems such models are computationally expensive to simulate, which can make optimisation problems, such as optimal control or parameter inference, prohibitively challenging. Here, we consider a class of multiscale population models that incorporate population-level mechanisms while remaining faithful to the underlying stochasticity at the single-cell level and the interplay between these two scales. To address the complexity, we study an order-reduction approximations based on the distribution moments. Since previous moment-closure work has focused on the single-cell kinetics, extending these techniques to populations models prompts us to revisit old observations as well as tackle new challenges. In this extended multiscale context, we encounter the previously established observation that the simplest closure techniques can lead to non-physical system trajectories. Despite their poor performance in some systems, we provide an example where these simple closures outperform more sophisticated closure methods in accurately, efficiently, and robustly solving the problem of optimal control of bioproduction in a microbial consortium model.

1 Introduction

Stochastic chemical kinetics lead to cell-to-cell variability within an isogenic population of cells. This can manifest in heterogeneous cell behaviour, such as response to stimuli or cell-fate decisions [3, 7, 18, 49]. Despite a thoroughly mechanistic understanding of the behaviour of individual cells and communities [50] many population models, particularly for the purposes of control, neglect this heterogeneity due to the complexity it introduces [16, 17]. When this nonuniformity is ignored the resulting dynamics and optimal controls can deviate significantly from the ideal performance [31].

Multiscale models that describe evolving populations of stochastic individual cells pose significant analytical and numerical difficulty, which is exacerbated when trying to optimise such systems. This motivates order-reduction techniques that can mitigate the complexity while retaining sufficient model accuracy. Moment-closure techniques have been a popular order-reduction approach that reduce computational complexity although their use for system optimisation has been limited. For instance, moment-closure techniques are well studied in the chemical kinetics literature [13, 22, 37, 43, 44, 45, 47, 48, 56, and references therein]. Moment closures have also been studied in the context of population balance equations used in aerosol modeling to resolve the evolution of particle distributions under an extensive array of physical phenomena such as evaporation, nucleation, growth, coagulation, and complex mixing [32, 33, 34, 40, 57].

In this work, we focus on heterogeneous population dynamics and their optimisation. Our contribution extends these previous studies in several ways. The models studied here are designed for growing populations of cells that undergo population-level processes while remaining faithful to the underlying stochasticity of single-cell chemical kinetics. This multiscale model is a significant departure from the single-cell perspective [29]. Moreover, much

---

*davin.lunz@inria.fr

previous moment-closure work has focused exclusively on simulating system evolution, whereas we consider the optimisation of such systems. We demonstrate that some techniques that successfully simulate system evolution do not provide a robust basis for system optimisation. This emphasises the need for novel moment-closure methods in this multiscale context that may be used for system optimisation.

Here, we study a class of PDE models and seek reduced-order models that preserve the heterogeneity in the original models. We approximate the moment hierarchy of the solution, which reduces a PDE to a system of ODEs by multiplying the governing equation by monomial of the state and integrating over the state space. This ODE system representation preserves the influence of the heterogeneity while significantly reducing the complexity by enveloping the state space. In general, this induces an infinite hierarchy of coupled moment equations, as the dynamics of each moment depend on higher-order moments. For practical purposes, such as numerical simulation, this system must be truncated at finite order and the higher-order terms beyond the truncation order must be approximated by a closure rule. We refer to the resulting finite system of moment equations as the moment-closure approximation. In contrast to previous work, where the same class of PDE models are studied alongside moment-closure approximations up to first order [31], we study moment closures of arbitrarily high order. As we will demonstrate, retaining orders above the first allows us to preserve heterogeneous features not accounted for in the lower-order (homogeneous) models.

In this multiscale setting, we encounter the well-established result that the simple moment-closure technique of approximating the truncated moments by zero can lead to non-physical dynamics while more sophisticated moment-closure approaches can successfully reproduce the exact dynamics. Somewhat counter-intuitively, we study the optimal control of a popular bioproduction system and demonstrate that the sophisticated moment closures fail where the simple moment closure provides robust convergence to give excellent control performance. This example suggests that the naive approach ought not be abandoned too hastily.

In some previous work, reaction propensities are assumed to be of polynomial form so as to provide a self-contained hierarchy of moment equations and avoid non-trivial approximation that introduces both complexity and an additional source of error. However, such simplifying assumptions may limit the scope and applicability of previous methods, leaving important applications beyond the reach of the existing methodology. For example, some non-polynomial functional forms have biological relevance, such as the Hill functional form, which is ubiquitous in biochemistry, with applications ranging from pharmacology to enzyme kinetics and gene expression models.

This problem has been previously addressed by either assuming rational functions [35] or Taylor expanding nonlinear functions [2, 5, 13, 19, 22, 24]. However, we show that, in many practical scenarios, these previous approaches are either infeasible or may produce less robust optimisation convergence. In this work, we derive the moment hierarchies using systematic polynomial approximations of arbitrary nonlinear forms. This approach does not assume that the propensities are rational functions, and provides a polynomial approximation that, as opposed to the Taylor expansion, which is only locally accurate, provides an approximation that covers the state space more broadly. The Weierstrass theorem [10, Ch. 6] (that any continuous function on a closed interval can be uniformly approximated with arbitrary precision by a polynomial function) suggests that polynomial approximations are a promising direction. Nevertheless, choosing an appropriate approximation can be challenging: we provide an example in which the closeness of the polynomial approximation is less important than other features, such as preserving monotonicity of the original function.

The remainder of the paper is organised as follows. In section 2 we introduce a modular class of population models with dynamics grounded in stochastic individual members. In section 3 we derive an associated hierarchy of approximate moment equations. In section 4 we discuss a selection of moment-closure techniques to limit the hierarchy to a finite system. We then study three examples. In sections 5 and 6, we study birth–death–growth and growth–fragmentation models, respectively, where simple moment closures do not perform adequately. In section 7, we study a microbial consortium model where only the simplest moment closure works to solve the bioproduction optimal control problem. Finally, we discuss the implications of our results and future directions in section 8.

2 Heterogeneous and modular model class

We begin by considering a collection of *continuum* quantities within each cell, such as levels of a protein of interest or a transcription factor. We denote the jth quantity x_j and the vector of the entire collection $\boldsymbol{x} = (x_1, \ldots, x_d) \in \mathbb{R}_+^d$. We then consider distinct *discrete* classes of cells, with cells in a given class being indistinguishable. Cell classes may represent different genetic constructs or simply distinct states of an identical construct. Our interest is in the dynamics of populations of large numbers of cells, and the primary object we study is the (expected) population density of each class over the continuum quantities. Importantly, heterogeneity at the single-cell level depends on the stochastic chemical kinetics, not the population size, and therefore persists in large populations [29]. We denote the population density of cells of class k over the continuum quantities $\boldsymbol{x}$ at time t by $p_k(\boldsymbol{x}, t)$. We are interested in models governing the evolution of the collection of population densities in all states, $\{p_k(\boldsymbol{x},t)\}_k$, of the form [31]

$$\frac{\partial}{\partial t}p_k(\boldsymbol{x},t) = \text{Population growth} + \text{Population dilution} + \text{Discrete dynamics} + \text{Continuum dynamics}, \tag{1a}$$

$$p_k(\boldsymbol{x},0) = p_{0k}(\boldsymbol{x}), \tag{1b}$$

for $k = 1, \ldots, \mathcal{K}$. Each term on the right-hand side of (1) contributes to the rate of change of the density of cells of class k with internal state $\boldsymbol{x}$, and thus each may depend on both k and $\boldsymbol{x}$, as well as time t.

What is the relationship between these contributions on the right-hand side of (1)? The first two terms capture population-level mechanisms, describing how the number of cells changes. The final two terms capture how the internal state of individual cells evolve. From this angle, the multiscale nature of the model is clearly manifest. The two scales are coupled due to the population-level processes depending on the cell states.

The discrete and continuum state spaces illustrate the hybrid nature of this approach: some states remain fully discrete, such as cell type, while others are fully continuous, such as concentration of a substance. This is in contrast to other hybrid approaches. For example, time-scale separation can be leveraged by treating fast and slow processes differently, or state-scale separation is leveraged to deal with low copy numbers differently to high copy numbers. We refer the reader to [29] for a more thorough overview of different hybrid approaches.

We now detail a collection of examples for each component. These are modeling pieces that may be combined together as necessary to forge a wide array of models, as we will subsequently demonstrate.

2.1 Population growth

The population growth refers to the processes by which the cells proliferate. A simple and classical example is exponential growth. If the continuum quantities $\boldsymbol{x}$ represent *concentrations* that remain essentially constant over cell division events [39], then the rate of change of cell density due to growth may be governed by a law of the form

$$\frac{\partial}{\partial t}p_k(\boldsymbol{x},t) = g_k(\boldsymbol{x},t)p_k(\boldsymbol{x},t) + (\text{Non-growth sources}), \tag{2}$$

where the growth rate $g_k(\boldsymbol{x},t)$ exhibits dependence on the states k and $\boldsymbol{x}$ as well as time t.

An alternative is to consider the continuum states $\boldsymbol{x}$ to represent (scaled) copy numbers. In this case, cell division events cause the state $\boldsymbol{x}$ to be partitioned and shared between the two daughter cells, which is described by a fragmentation process. We define the set of states $\boldsymbol{x} \in \mathbb{R}_+^d$ with each component of $\boldsymbol{x}$ no greater than each corresponding component of some parameter $\bar{\boldsymbol{x}}$, which we denote $\boldsymbol{0} \leq \boldsymbol{x} \leq \bar{\boldsymbol{x}} := [0, \bar{x}_1] \times \cdots \times [0, \bar{x}_d]$ where $\boldsymbol{0} = (0, \ldots, 0) \in \mathbb{N}_0^d$ is the d-dimensional vector of zeros. Similarly, $\boldsymbol{x} \geq \bar{\boldsymbol{x}}$ denotes the set of $\boldsymbol{x} \in \mathbb{R}_+^d$ where each component of $\boldsymbol{x}$ is no less than its counterpart in $\bar{\boldsymbol{x}}$. The rate of change of cell density is then governed by

$$\frac{\partial}{\partial t}p_k(\boldsymbol{x},t) = -g_k(\boldsymbol{x},t)p_k(\boldsymbol{x},t) + 2\int_{\hat{\boldsymbol{x}} \geq \boldsymbol{x}} g_k(\hat{\boldsymbol{x}},t)p_k(\hat{\boldsymbol{x}},t)\theta_k(\boldsymbol{x} \mid \hat{\boldsymbol{x}})\,\mathrm{d}\hat{\boldsymbol{x}} + (\text{Non-growth sources}), \tag{3}$$

where the growth rate is still $g_k(\boldsymbol{x},t)$ and $\theta_k(\boldsymbol{x} \mid \hat{\boldsymbol{x}})$ represents the probability density that, for a given daughter cell, a mother cell in state $\hat{\boldsymbol{x}}$ divides to produce a daughter in state $\boldsymbol{x}$. In contrast to the growth term in (2), representing an exponential increase in population density at state $\boldsymbol{x}$ due to cell duplication, the first term on the right-hand side of the copy-number form (3) has a leading minus sign. This reflects the fact that a cell division event to a mother cell in state $\boldsymbol{x}$ causes the loss of population density at this state. This loss is balanced by two new cell states, which explains the factor of two multiplying the integral term.

We require that θ_k be a symmetric probability density:

$$\int_{\boldsymbol{0} \leq \boldsymbol{x} \leq \hat{\boldsymbol{x}}} \theta_k(\boldsymbol{x} \mid \hat{\boldsymbol{x}})\,\mathrm{d}\boldsymbol{x} = 1, \qquad \theta_k(\boldsymbol{x} \mid \hat{\boldsymbol{x}}) = \theta_k(\hat{\boldsymbol{x}} - \boldsymbol{x} \mid \hat{\boldsymbol{x}}). \tag{4}$$

Assumptions (4) guarantee that the fragmentation contributes an increase in the total number of cells per unit time while conserving the total protein copy number. To derive the moment hierarchy, we will require the additional assumption of self-similarity

$$\theta_k(\boldsymbol{x} \mid \hat{\boldsymbol{x}}) = \hat{\boldsymbol{x}}^{-\boldsymbol{1}}\Theta_k(\boldsymbol{x} \oslash \hat{\boldsymbol{x}}), \tag{5}$$

for some probability density $\Theta_k : \boldsymbol{0} \leq \boldsymbol{y} \leq \boldsymbol{1} \to \mathbb{R}_+$ where $\boldsymbol{1} = (1, \ldots, 1) \in \mathbb{N}_0^d$ is the d-dimensional vector of ones and we introduce the Hadamard product and division, defined respectively by

$$\boldsymbol{x} \odot \boldsymbol{y} = (x_1 y_1, \ldots, x_d y_d), \qquad \boldsymbol{x} \oslash \boldsymbol{y} = \left(\frac{x_1}{y_1}, \ldots, \frac{x_d}{y_d}\right). \tag{6}$$

To see that Θ_k is a probability density, note that, by using the change of variables $\boldsymbol{y} := \boldsymbol{x} \oslash \hat{\boldsymbol{x}}$, the density condition in (4) takes the form

$$1 = \int_{\mathbf{0} \le \boldsymbol{x} \le \hat{\boldsymbol{x}}} \theta_k(\boldsymbol{x} \mid \hat{\boldsymbol{x}}) \, \mathrm{d}\boldsymbol{x} = \hat{\boldsymbol{x}}^{\mathbf{1}} \int_{\mathbf{0} \le \boldsymbol{y} \le \mathbf{1}} \theta_k(\hat{\boldsymbol{x}} \odot \boldsymbol{y} \mid \hat{\boldsymbol{x}}) \, \mathrm{d}\boldsymbol{y} = \int_{\mathbf{0} \le \boldsymbol{y} \le \mathbf{1}} \Theta_k(\boldsymbol{y}) \, \mathrm{d}\boldsymbol{y}. \tag{7}$$

For $\mathbf{0} \le \boldsymbol{y} \le \mathbf{1}$, the symmetry condition in (4) takes the form

$$\Theta_k(\boldsymbol{y}) = \Theta_k(\mathbf{1} - \boldsymbol{y}). \tag{8}$$

2.2 Population dilution

In many practical scenarios, the population is diluted to preserve healthy growth conditions. For example, bioreactors have modes of continuous operation that allow fresh media to be introduced into the bioreactor, and the existing solution diluted to remove toxins and biproducts as well as maintain an equilibrium population density. This allows longer operation, reducing the burden of frequently resetting the bioreactor, and simplifies the modeling as it allows the colony and nutrients to remain in a steady growth phase [42].

We consider the turbidostat operation mode, where the dilution is tuned in real time so as to maintain a constant optical density. Taking the optical density as a proxy for the population density, we model this contribution via the dilution rate, $\Lambda(t)$,

$$\frac{\partial}{\partial t} p_k(\boldsymbol{x}, t) = -\Lambda(t) p_k(\boldsymbol{x}, t) + (\text{Non-dilution sources}), \tag{9}$$

where $\Lambda(t)$ does not depend on k or $\boldsymbol{x}$, but does depend on the population density as follows. Integrating (1) over the state space $\boldsymbol{x} \in \mathbb{R}_+^d$ and summing over all discrete states $k = 1, \ldots, \mathcal{K}$, the discrete and continuum dynamics cancel as they are *conservative*; describing how members of the population change their states k and $\boldsymbol{x}$ without changing the total population mass. In this case, where all changes in population mass stem from the "Population growth" terms, it follows that

$$\Lambda(t) = \frac{\displaystyle\sum_{k=1}^{\mathcal{K}} \int_{\mathbb{R}_+^d} [\text{Population growth}]_k(\boldsymbol{x}, t) \, \mathrm{d}\boldsymbol{x}}{\displaystyle\sum_{k=1}^{\mathcal{K}} \int_{\mathbb{R}_+^d} p_k(\boldsymbol{x}, t) \, \mathrm{d}\boldsymbol{x}}, \tag{10}$$

where we have shown the explicit dependence of the population growth contributions on the states k and $\boldsymbol{x}$ and time t. The turbidostat dilution rate (10) is simply the mean growth rate, which is precisely the balance required to preserve a constant total population mass. Moreover, since the denominator in (10) is constant, we may assume, without loss of generality, that it is unity. This is equivalent to rescaling the population densities $p_k(\boldsymbol{x}, t)$ by this constant value. This gives a simpler form for the dilution rate, namely

$$\Lambda(t) = \sum_{k=1}^{\mathcal{K}} \int_{\mathbb{R}_+^d} [\text{Population growth}]_k(\boldsymbol{x}, t) \, \mathrm{d}\boldsymbol{x}. \tag{11}$$

2.3 Discrete dynamics

Discrete dynamics refers to the change of state of a cell in class k to some other class ℓ, at a rate denoted by $c_{k\ell}(\boldsymbol{x}, t)$, whereby

$$\frac{\partial}{\partial t} p_k(\boldsymbol{x}, t) = -p_k(\boldsymbol{x}, t) \sum_{\ell=1}^{\mathcal{K}} c_{k\ell}(\boldsymbol{x}, t) + \sum_{\ell=1}^{\mathcal{K}} c_{\ell k}(\boldsymbol{x}, t) p_\ell(\boldsymbol{x}, t) + (\text{Non-discrete sources}). \tag{12}$$

The discrete states might represent the copy number of a species produced in numbers below what would justify a continuum approximation [28, 29] or a binary internal state such as governed by binding kinetics. In such cases the discrete dynamics describe stochastic single-cell chemical kinetics. In the current formulation, the copy-number paradigm for continuum species does not carry over to dividing discrete species, however, this is an immediate extension.

2.4 Continuum dynamics

Continuum dynamics refers to the change of state of a cell in state $\boldsymbol{x}$ to some other state $\boldsymbol{y}$. Note that the label "continuum" describes the fact that the dynamics occur within the *continuum* state space $\mathbb{R}_+^d$ and not the discrete state space. However, the change caused to a single cell's state may be discontinuous. For example, the evolution of the continuum state $\boldsymbol{x}$ under a birth–death process with rate $r_k(\boldsymbol{x}, t) \geq 0$ is described by the Fokker–Planck operator

$$\frac{\partial}{\partial t} p_k(\boldsymbol{x}, t) = -\boldsymbol{e}_k \cdot \nabla \left[r_k(\boldsymbol{x}, t) p_k(\boldsymbol{x}, t) \right] + \frac{1}{2\Omega} \boldsymbol{e}_k^\top \nabla^2 \left[r_k(\boldsymbol{x}, t) p_k(\boldsymbol{x}, t) \right] \boldsymbol{e}_k + (\text{other sources}), \tag{13}$$

where $\boldsymbol{e}_k \in \mathbb{Z}^d$ is a vector representing the number of reactant molecules minus the number of product molecules of each continuum species [29], ∇^2 denotes the Hessian, and Ω is the characteristic system size [28]. The operator is associated with the zero normal-flux boundary condition

$$(\boldsymbol{e}_k \cdot \boldsymbol{n}) \left\{ r_k(\boldsymbol{x}, t) p_k(\boldsymbol{x}, t) - \frac{1}{2\Omega} \boldsymbol{e}_k \cdot \nabla \left[r_k(\boldsymbol{x}, t) p_k(\boldsymbol{x}, t) \right] \right\} = 0, \qquad \boldsymbol{x} \in \partial \mathbb{R}_+^d, \tag{14}$$

where $\boldsymbol{n}$ denotes the outward-facing normal to the boundary. There may be many such processes occurring simultaneously on the state k, in which case we sum over all the associated Fokker–Planck operators and boundary conditions. This operator may be written in divergence form, from which its conservative nature is apparent, as done in Appendix A.2.

In many biologically relevant scenarios, production in "bursts" provides a more realistic description of the underlying production mechanism. For example, in cells where mRNA molecules are short-lived due to rapid degradation and, simultaneously, protein translation is rapid, we may consider protein production to occur in instantaneous "bursts" of geometrically distributed size [27]. The continuum dynamics take the form

$$\begin{aligned} \frac{\partial}{\partial t} p_k(\boldsymbol{x}, t) = -f_k(\boldsymbol{x}, t) p_k(\boldsymbol{x}, t) + \|\boldsymbol{e}_k\| \int_{\boldsymbol{x} - z\boldsymbol{e}_k \in \mathbb{R}_+^d} f_k(\boldsymbol{x} - z\boldsymbol{e}_k, t) p_k(\boldsymbol{x} - z\boldsymbol{e}_k, t) Q_k(\boldsymbol{x} - z\boldsymbol{e}_k, z\|\boldsymbol{e}_k\|) \, \mathrm{d}z \\ + (\text{other sources}), \end{aligned} \tag{15}$$

where $\boldsymbol{e}_k \in \mathbb{Z}^d$ again represents the number of reactant molecules minus the number of product molecules, $f_k(\boldsymbol{x}, t)$ denotes the rate of production bursts, and $Q_k(\boldsymbol{x}, y)$ denotes the probability density, characteristically of exponential form, that the production process in a cell of state $\boldsymbol{x}$ yields a state $\boldsymbol{x} + y\boldsymbol{e}_k / \|\boldsymbol{e}_k\|$. We thus require that, for all $\boldsymbol{x}$,

$$\int_0^\infty Q_k(\boldsymbol{x}, y) \, \mathrm{d}y = 1. \tag{16}$$

Here too, if several such process occur simultaneously these are to be summed.

There are no boundary conditions to be imposed with the burst operator, however, the formulation (15) implicitly imposes boundary conditions. The present formulation assumes that all components of the vector $\boldsymbol{e}_k$ are non-negative. Were this not the case, the first term on the right-hand side of (15) would need to be modulated by a coefficient representing the fraction of valid jumps: $v_k(\boldsymbol{x}) := \|\boldsymbol{e}_k\| \int_{\boldsymbol{x} + z\boldsymbol{e}_k \in \mathbb{R}_+^d} Q_k(z\|\boldsymbol{e}_k\|) \, \mathrm{d}z$. This would disallow jumps that use "exhausted" continuum species (that is, jumps to states $\boldsymbol{x}$ with at least one negative component) and instead leave the state unchanged. This treatment can be handled in the present formulation by simply absorbing the coefficient $v_k(\boldsymbol{x})$ into the rate $f_k(\boldsymbol{x}, t)$. A more physically relevant model would place the fraction $1 - v_k(\boldsymbol{x})$ of invalid jumps at the boundary, however, for the sake of simplicity, we will not account for this.

2.5 Model synopsis

Before proceeding to discuss approximation techniques for the model class introduced in this section, it is worth reflecting conceptually on the model. It is instructive to pose the question: what is the connection between the model presented here and traditional stochastic chemical kinetics? Answering this question will help shed light on the nature of the model and reveal how the model structure addresses several key issues unaddressed by other modelling approaches.

If we neglect population growth and dilution, as well as the continuum dynamics, the model reduces exactly to the chemical master equation, capturing the law of (discrete) stochastic chemical kinetics. Reinstating the continuum dynamics introduces a representation that allows us to leverage tools from the numerical analysis of PDEs. In real-world scenarios the discrete system size is typically large (copy numbers are often tens of thousands, and can sometimes be in the millions). Especially when multiple species are considered, the system size required in this direct discrete approach quickly becomes infeasible for numerical simulation. At the same time, as the system size increases, the continuum formulation becomes more accurate [28]. Crucially, the continuum representation provides a systematic framework in which the discretisation can remain numerically feasible and accurate [29]. From this perspective, the continuum formulation provides a systematic method to derive the system dynamics when several states are "lumped" together. While some species may occur in exceedingly large numbers, others may not require this treatment. Therefore, retaining both the discrete description alongside the continuum representation allows a hybrid model that can simultaneously cater to both these modeling needs. Nevertheless, even the continuum formulation suffers from the curse of dimensionality and, especially when several species are required, the system size can still sometimes be prohibitively large. This motivates order-reduction methods that we will introduce in the next section.

Therefore, without population growth, the hybrid model may be described as being based on the exact discrete chemical master equation, with an extension to include a continuum representation for abundant species. When also considering the population growth and dilution the model goes one step beyond the chemical master equation perspective in considering a population of individual stochastic cells, rather than just the stochastic behaviour of a single cell. This imbues the model with a different analytical structure than that of master equation models: the distribution is a population density but not necessarily a probability density [29]. Conceptually, when the population growth is accounted for, the model can be seen as the expected population density of a population undergoing stochastic growth events, as derived in detail in other work [12, 30, 52]. Considering the full distribution of populations over these stochastic growth events for any real-world system is computationally intractable. Studying only the expected population produces the model we pose here, which strikes a balance between retaining the important population heterogeneity [31] while retaining a more manageable state space size [12, 30].

Finally, with this concrete model overview in mind, we may look at real-world scenarios where these models (and the associated order-reduction tools) can be applied. In several experimental studies, a strong interplay between heterogeneity within a population (born of stochastic chemical kinetics) and population level processes, such as state-dependent growth rates, has been observed [1, 9, 11, 20, 38, 51]. The need to represent the single-cell heterogeneity while simultaneously coupling it to the population-level dynamics is thus becoming more established. We thus foresee fruitful opportunity for this model class to provide a unifying modeling framework for analysis of such real-world data.

3 Moment hierarchy

The analysis and optimal control of the modular PDE models introduced in section 2 is formidably challenging. The computational cost of their numerical simulation and optimisation quickly becomes prohibitive with increasing resolution and dimension, motivating dimension reduction techniques.

Taking the components introduced in section 2, we derive the associated contributions to the moment hierarchy. We introduce the (scalar) moments

$$X_k^{\boldsymbol{i}}(t) := \int_{\mathbb{R}_+^d} \boldsymbol{x}^{\boldsymbol{i}} p_k(\boldsymbol{x}, t)\,\mathrm{d}\boldsymbol{x}, \tag{17}$$

for the multi-index $\boldsymbol{i} = (i_1, \ldots, i_d) \in \mathbb{N}_0^d$, where $\boldsymbol{x}^{\boldsymbol{i}} = \prod_{j=1}^d x_j^{i_j} \in \mathbb{R}_+$ and we write $|\boldsymbol{i}| := \sum_{j=1}^d i_j$. The governing equation of each moment $X_k^{\boldsymbol{i}}(t)$ is found by multiplying the PDE governing $p_k(\boldsymbol{x}, t)$ by $\boldsymbol{x}^{\boldsymbol{i}}$ and integrating over the state space. The details of these calculations appear in Appendix A, and in this section we outline the results.

To produce a closed hierarchy of moments, we approximate the non-polynomial functions of state on the right-hand side of (1) by a polynomial form. So for a function $g_k(\boldsymbol{x}, t)$, we take the $N(g_k)$-degree approximation, denoted by

$$g_k(\boldsymbol{x}, t) \approx \sum_{|\boldsymbol{j}| \le N(g_k)} g_{k,\boldsymbol{j}}(t) \boldsymbol{x}^{\boldsymbol{j}}, \tag{18}$$

where we use the multi-index notation $\boldsymbol{j} \in \mathbb{N}_0^d$ for which $\boldsymbol{x}^{\boldsymbol{j}} = x_1^{j_1} \cdots x_d^{j_d} \in \mathbb{R}$ is a scalar value. This step raises the question of how to select a polynomial approximation. Later, with application to a concrete example, we discuss important considerations in this choice.

3.1 Population growth

The growth law in the concentration paradigm (2) contributes to the moments via

$$\begin{aligned}\frac{\mathrm{d}}{\mathrm{d}t}X_k^{\boldsymbol{i}}(t) &= \int_{\mathbb{R}_+^d} \boldsymbol{x}^{\boldsymbol{i}} g_k(\boldsymbol{x},t) p_k(\boldsymbol{x},t)\,\mathrm{d}\boldsymbol{x} + (\text{Non-growth sources})\\ &\approx \sum_{|\boldsymbol{j}|\le N(g_k)} g_{k,\boldsymbol{j}}(t)\int_{\mathbb{R}_+^d} \boldsymbol{x}^{\boldsymbol{i}+\boldsymbol{j}} p_k(\boldsymbol{x},t)\,\mathrm{d}\boldsymbol{x} + (\text{Non-growth sources})\\ &= \sum_{|\boldsymbol{j}|\le N(g_k)} g_{k,\boldsymbol{j}}(t) X_k^{\boldsymbol{i}+\boldsymbol{j}}(t) + (\text{Non-growth sources}).\end{aligned} \tag{19}$$

In the copy-number paradigm, we show in Appendix A that, assuming self-similarity (5), the moment equations take the form

$$\frac{\mathrm{d}}{\mathrm{d}t}X_k^{\boldsymbol{i}}(t) = (2\Theta_k^{\boldsymbol{i}} - 1)\sum_{|\boldsymbol{j}|\le N(g_k)} g_{k,\boldsymbol{j}}(t) X_k^{\boldsymbol{i}+\boldsymbol{j}}(t) + (\text{Non-growth sources}), \tag{20}$$

for

$$\Theta_k^{\boldsymbol{i}} := \int_{\boldsymbol{0}\le\boldsymbol{y}\le\boldsymbol{1}} \boldsymbol{y}^{\boldsymbol{i}}\Theta_k(\boldsymbol{y})\,\mathrm{d}\boldsymbol{y}. \tag{21}$$

Note from (7) that the zeroth-order contribution $\Theta_k^{\boldsymbol{0}} = 1$ for $\boldsymbol{0} = (0,\dots,0)$. This demonstrates how the moment hierarchy preserves the form of the total growth rate: for $\boldsymbol{i} = \boldsymbol{0}$, the right-hand sides of (19) and (20) are identical.

3.2 Population dilution

The turbidostat contribution (9), which maintains a constant population mass, is approximated by

$$\frac{\mathrm{d}}{\mathrm{d}t}X_k^{\boldsymbol{i}}(t) = -\Lambda(t)X_k^{\boldsymbol{i}}(t) + (\text{Non-dilution sources}), \tag{22}$$

where the turbidostat dilution rate $\Lambda(t)$ given in (11) may be expressed self-consistently as the sum of the growth contributions of zeroth order $\boldsymbol{i} = \boldsymbol{0}$. In both the concentration (19) and copy-number (20) paradigms the zeroth-order contributions are identical, therefore, in both cases,

$$\Lambda(t) = \sum_{k=1}^{\mathcal{K}}\sum_{|\boldsymbol{j}|\le N(g_k)} g_{k,\boldsymbol{j}}(t) X_k^{\boldsymbol{j}}(t). \tag{23}$$

It follows that, in turbidostat mode, the total population mass $\sum_{k=1}^{\mathcal{K}} X_k^{\boldsymbol{0}}(t)$ remains constant in the moment-closure approximation.

3.3 Discrete dynamics

The discrete dynamics (12) lend the contributions

$$\frac{\mathrm{d}}{\mathrm{d}t}X_k^{\boldsymbol{i}}(t) = -\sum_{\ell=1}^{\mathcal{K}}\sum_{|\boldsymbol{j}|\le N(c_{k\ell})} c_{k\ell,\boldsymbol{j}}(t) X_k^{\boldsymbol{i}+\boldsymbol{j}}(t) + \sum_{\ell=1}^{\mathcal{K}}\sum_{|\boldsymbol{j}|\le N(c_{\ell k})} c_{\ell k,\boldsymbol{j}}(t) X_\ell^{\boldsymbol{i}+\boldsymbol{j}}(t) + (\text{Non-discrete sources}). \tag{24}$$

Here too the conservation property of the discrete dynamics is preserved: summing (24) over k we find that $\sum_{k=1}^{\mathcal{K}} X_k^{\boldsymbol{i}}(t)$ is changed only by non-discrete sources.

3.4 Continuum dynamics

In Appendix A we show that the contributions stemming from the Fokker–Planck terms (13) take the form

$$\begin{aligned}\frac{\mathrm{d}}{\mathrm{d}t}X_k^{\boldsymbol{i}}(t) \approx{}& \sum_{\ell=1}^{d} i_\ell e_{k,\ell}\sum_{|\boldsymbol{j}|\le N(r_k)} r_{k,\boldsymbol{j}}(t) X_k^{\boldsymbol{i}-\boldsymbol{v}_\ell+\boldsymbol{j}}(t) + \frac{1}{2\Omega}\sum_{\ell=1}^{d}\sum_{m=1}^{d} i_\ell(i_m - \delta_{\ell m}) e_{k,\ell} e_{k,m}\sum_{|\boldsymbol{j}|\le N(r_k)} r_{k,\boldsymbol{j}}(t) X_k^{\boldsymbol{i}-\boldsymbol{v}_\ell-\boldsymbol{v}_m+\boldsymbol{j}}(t)\\ &+ (\text{other sources}),\end{aligned} \tag{25}$$

where $\delta_{\ell m}$ is the Kronecker Delta function, which takes the value one when $\ell = m$ and zero otherwise, and $\boldsymbol{v}_\ell$ denotes the vector of zeros except for the ℓth component whose value is one. The moment approximation (25) of the Fokker–Planck terms has no zeroth-order ($\boldsymbol{i} = \boldsymbol{0}$) contribution, thus preserving the conservation property that $X_k^{\boldsymbol{0}}(t)$ is changed only by non-continuum sources.

The moments for the bursty production (15) are calculated in Appendix A, where we find that

$$\frac{\mathrm{d}}{\mathrm{d}t}X_k^{\boldsymbol{i}}(t) = \sum_{\boldsymbol{j}<\boldsymbol{i}} b_{\boldsymbol{i},\boldsymbol{j}}\boldsymbol{e}_k^{\boldsymbol{i}-\boldsymbol{j}}\|\boldsymbol{e}_k\|^{-|\boldsymbol{i}-\boldsymbol{j}|}\int_{\mathbb{R}_+^d}\boldsymbol{x}^{\boldsymbol{j}}Q_{k,|\boldsymbol{i}-\boldsymbol{j}|}(\boldsymbol{x})f_k(\boldsymbol{x},t)p_k(\boldsymbol{x},t)\,\mathrm{d}\boldsymbol{x} + (\text{other sources}), \tag{26}$$

where the coefficients $b_{\boldsymbol{i},\boldsymbol{j}}$ are defined by (81), and we have defined, for $j \in \mathbb{N}_0$,

$$Q_{k,j}(\boldsymbol{x}) := \int_0^\infty y^j Q_k(\boldsymbol{x},y)\,\mathrm{d}y. \tag{27}$$

Denoting the polynomial approximation

$$Q_{k,j}(\boldsymbol{x}) \approx \sum_{|\boldsymbol{\ell}|\le jN(Q_{k,j})} w_{k,j,\boldsymbol{\ell}}\boldsymbol{x}^{\boldsymbol{\ell}}, \tag{28}$$

we see that

$$\frac{\mathrm{d}}{\mathrm{d}t}X_k^{\boldsymbol{i}}(t) \approx \sum_{\boldsymbol{j}<\boldsymbol{i}} b_{\boldsymbol{i},\boldsymbol{j}}\boldsymbol{e}_k^{\boldsymbol{i}-\boldsymbol{j}}\|\boldsymbol{e}_k\|^{-|\boldsymbol{i}-\boldsymbol{j}|}\sum_{|\boldsymbol{\ell}|\le|\boldsymbol{i}-\boldsymbol{j}|N(q_k)}\ \sum_{|\boldsymbol{m}|\le N(f_k)} w_{k,|\boldsymbol{i}-\boldsymbol{j}|,\boldsymbol{\ell}}f_{k,\boldsymbol{m}}(t)X_k^{\boldsymbol{j}+\boldsymbol{\ell}+\boldsymbol{m}}(t) + (\text{other sources}). \tag{29}$$

The moment approximation (29) of the bursty production terms has no zeroth-order contribution (when $\boldsymbol{i} = \boldsymbol{0}$ the right-hand side of (29) vanishes because there are no multi-indices $\boldsymbol{j} < \boldsymbol{i}$), thus guaranteeing the conservation property that $X_k^{\boldsymbol{0}}(t)$ is changed only by non-continuum sources.

It is instructive to consider the concrete example of the typical exponential jump distribution, which is obtained in the continuum limit of geometrically distributed burst sizes introduced in section 2.4, and matches experimentally observed burst sizes [14]. The exponential kernel takes the form

$$Q_k(\boldsymbol{x},y) = \frac{\mathrm{e}^{-y/q_k(\boldsymbol{x})}}{q_k(\boldsymbol{x})}, \tag{30}$$

for a (possibly state-dependent) mean burst size q. The kernel satisfies (16), $Q_{k,0}(\boldsymbol{x}) = 1$, and gives, by integrating by parts, the recursive relation $Q_{k,j}(\boldsymbol{x}) = jq(\boldsymbol{x})Q_{k,j-1}(\boldsymbol{x})$ for $j \ge 1$. It follows that

$$Q_{k,j}(\boldsymbol{x}) = j!q_k(\boldsymbol{x})^j. \tag{31}$$

Taking the polynomial approximation of q_k, we then see that

$$Q_{k,j}(\boldsymbol{x}) \approx j!\left(\sum_{|\boldsymbol{\ell}|\le N(q_k)} q_{k,\boldsymbol{\ell}}\boldsymbol{x}^{\boldsymbol{\ell}}\right)^j = \sum_{|\boldsymbol{\ell}|\le jN(q_k)} w_{k,j,\boldsymbol{\ell}}\boldsymbol{x}^{\boldsymbol{\ell}}, \tag{32}$$

for some coefficients $w_{k,j,\boldsymbol{\ell}}$.

3.5 Initial conditions

The moments inherit their initial conditions from the moments of the initial density (1b), that is,

$$X_k^{\boldsymbol{i}}(0) = \int_{\mathbb{R}_+^d}\boldsymbol{x}^{\boldsymbol{i}}p_{0k}(\boldsymbol{x})\,\mathrm{d}\boldsymbol{x}. \tag{33}$$

This concludes the derivation of the ODE components of the moment hierarchies from the components of the PDE model class. Before proceeding to discuss techniques to close the moment hierarchies, we briefly discuss the choice of a hybrid model structure with moment closures. Since we study moments over the continuum variables only, we could have posed a fully discrete model to begin with. This would have avoided errors associated with pursuing the continuum approximation, while still providing a closed moment hierarchy as above. As detailed in section 2.5, one major advantage to the continuum formulation is that it brings within reach simulation of realistic system sizes. This provides an important advantage for benchmarking, since we can compare results of the full system versus the moment hierarchies for realistic system sizes. Moreover, in Appendix B we study the difference between the moment hierarchies derived for a simple example using analogous discrete and Fokker–Planck formulations. We show that the continuum system is an asymptotically small perturbation from the discrete version. In addition to shedding light on the discrete moment hierarchy, this result demonstrates that, in practice, when system size is large, the error from using the continuum formulation is expected to be entirely negligible and can be safely ignored.

4 Moment closures

Equipped with the infinite moment hierarchies, we must decide how to close the moment equations so as to be able to solve a finite collection numerically. We will discuss three closure schemes.

The simplest thing to do is to consider all higher-order moments to be zero: for some N, set

$$X_k^{\boldsymbol{i}}(t) = 0, \qquad \text{for all } k \text{ and all } |\boldsymbol{i}| \geq N. \tag{34}$$

While this is straightforward, it implicitly relies on the assumption that the higher-order moments do not have an important influence on the lower-order moments. This is a very strong assumption, especially in the context of nonlinear functions subject to polynomial approximation. Nevertheless, we will discover that, despite its shortcomings, the zero closure, as we will call it, can be surprisingly useful.

A more appealing idea, for distributions concentrated near their mean, is to assume that the *central* higher-order moments vanish, that is,

$$\int_0^\infty \left(\boldsymbol{x} - \boldsymbol{X}_k(t)\right)^{\boldsymbol{i}} p_k(x,t)\,\mathrm{d}x = 0, \qquad \text{for all } k \text{ and all } |\boldsymbol{i}| \geq N, \tag{35}$$

where $\boldsymbol{X}_k(t)$ is the vector of means

$$\boldsymbol{X}_k(t) = \left(\frac{X_k^{\boldsymbol{v}_1}(t)}{X_k^{\boldsymbol{0}}(t)}, \ldots, \frac{X_k^{\boldsymbol{v}_d}(t)}{X_k^{\boldsymbol{0}}(t)}\right), \tag{36}$$

with $\boldsymbol{v}_i$ denoting the d-dimensional vector of zeros except the ith entry which is one. Performing the binomial expansion, the condition (35) gives the central closure, as we will call it. For example, in dimension $d = 1$, we obtain the formula

$$X_k^i(t) = -\sum_{j=0}^{i-1} \binom{i}{j} \left(-\frac{X_k^1(t)}{X_k^0(t)}\right)^{i-j} X_k^j(t), \qquad \text{for all } k \text{ and all } i \geq N. \tag{37}$$

Finally, we consider the zero-information closure [48]. At any point in time t, the distribution is assumed to be the distribution of maximum-entropy whose first N moments coincide with the given lower-order moments $\{X^i(t)\}_{i=0}^{N-1}$. By solving the constrained optimisation problem of maximising the entropy subject to the constraint of given moments, we may reconstruct the distribution, and, in turn, we may calculate the higher-order moments (a complete account is given in Ref. [48], and the maximum-entropy reconstruction code is available in the notebook of the code package published with this work). We will demonstrate that this technique can succeed where the previous closure methods fail, nevertheless, the reconstruction and subsequent moment calculation is nontrivial and costly, which makes them difficult to use in optimisation loops.

Armed with techniques to close the moment systems, we proceed to consider three examples: a birth–death single-cell model coupled to selective growth, a family of growth–fragmentation models, and a microbial consortium model. In the first two examples, we discuss simulating the moment equations using the three different closure schemes, while in the final example we seek to solve an optimal control problem of maximising bioproduction yield.

5 Birth–death–growth models

We begin with a birth–death process of a single species X, which models the single-cell reactions

$$\varnothing \xrightarrow{\lambda} \mathrm{X} \xrightarrow{\mu} \varnothing, \tag{38}$$

for the non-negative birth and death rates λ and μ, respectively, which may depend on the state.

In addition to the single-cell dynamics, there is a population-level selection due to a selective growth rate G that may also depend on the state. Under the continuum scaling [29], the population density is governed by

$$\frac{\partial}{\partial t}p(x,t) = G(x)p(x,t) - \frac{\partial}{\partial x}\left[(\lambda(x) - \mu(x))p(x,t)\right] + \frac{1}{2\Omega}\frac{\partial^2}{\partial x^2}\left[(\lambda(x) + \mu(x))p(x,t)\right], \qquad p(x,0) = p_0(x), \tag{39a}$$

for some initial distribution $p_0(x)$, and the zero normal flux boundary conditions

$$(\lambda(x) - \mu(x))p(x,t) - \frac{1}{2\Omega}\frac{\partial}{\partial x}\left[(\lambda(x) + \mu(x))p(x,t)\right] = 0, \qquad \text{at } x = 0 \text{ and as } x \to \infty. \tag{39b}$$

It will be convenient to choose the polynomial birth, death, and growth rates studied in Ref. [29] since analytical approximations are available in different limiting cases. These are given by

$$\lambda(x) = \Lambda x(1-x), \qquad \mu(x) = x, \qquad G(x) = gx, \tag{40}$$

where we assume $\Lambda > 1$ such that we are in the supercritical case (for $\Lambda \leq 1$, there is no state $x > 0$ that constitutes a metastable equilibrium for the single-cell stochastic dynamics).

It can be shown [29] that the large-time behaviour of the solution is to have a population distribution around a critical point $x = x_c$ and growing exponentially at a rate $G(x_c)$. Up to exponentially small corrections in the large system-size limit $\Omega \gg 1$, the distribution is

$$p(x,t) \sim \sqrt{\frac{a\Omega}{\pi}}\, \mathrm{e}^{G(x_c)t - a\Omega(x-x_c)^2}, \tag{41a}$$

where x_c is the unique (positive) point where the birth and death rates match, namely $\lambda(x_c) = \mu(x_c)$ at $x_c = 1 - 1/\Lambda$, and

$$a := -\frac{\lambda'(x_c) - \mu'(x_c)}{\lambda(x_c) + \mu(x_c)}, \tag{41b}$$

with the primes denoting derivatives. Since $x_c \in (0,1)$, the distribution is centred around a point for which the birth rate is positive. Multiplying (41) by x^i, integrating, we deduce that, up to exponentially small corrections, the long-term moments are of the form

$$\begin{aligned} X^i(t) &\sim \int_0^\infty x^i p(x,t)\,\mathrm{d}x \\ &\sim \frac{1}{\sqrt{\pi}(a\Omega)^{i/2}}\,\mathrm{e}^{G(x_c)t} \int_{-\infty}^{\infty} y^i \mathrm{e}^{-(y-y_c)^2}\,\mathrm{d}y \\ &\sim \frac{1}{\sqrt{\pi}(a\Omega)^{i/2}}\,\mathrm{e}^{G(x_c)t} \int_{-\infty}^{\infty} (z+y_c)^i \mathrm{e}^{-z^2}\,\mathrm{d}z \\ &= \frac{1}{\sqrt{\pi}}\,\mathrm{e}^{G(x_c)t} \sum_{j=0}^{i} \binom{i}{j} x_c^{i-j} (a\Omega)^{-j/2} \begin{cases} \Gamma\left(\frac{j+1}{2}\right), & j \text{ even}, \\ 0, & j \text{ odd}, \end{cases} \end{aligned} \tag{42}$$

where $y_c = x_c\sqrt{a\Omega}$ and Γ is the Gamma function. Notably, we see that $X^i(t) \propto \mathrm{e}^{G(x_c)t}$ for some constant of proportionality (that depends on i).

In addition to the large-time benchmark, we may also compute an analytical solution in the limiting case of $\Omega \to \infty$ where we neglect the second-order term in (39) to give the hyperbolic PDE

$$\frac{\partial}{\partial t}p(x,t) = G(x)p(x,t) - \frac{\partial}{\partial x}\left[(\lambda(x) - \mu(x))p(x,t)\right], \qquad p(x,0) = p_0(x), \tag{43a}$$

with zero normal flux boundary conditions

$$(\lambda(x) - \mu(x))p(x,t) = 0, \qquad \text{at } x = 0 \text{ and as } x \to \infty. \tag{43b}$$

This is a singular limit: far from x_c the solution of (39) will be well approximated by the solution of (43), however, in a vicinity of $x = x_c$, there will be a boundary layer where this approximation breaks down (and similarly if the initial distribution has steep gradients). Nevertheless, it is enlightening to study this reduced problem.

The hyperbolic PDE (43) may be solved by the method of characteristics. Substituting the particular forms (40) into (43), we find that characteristic curves satisfy

$$\frac{\mathrm{d}}{\mathrm{d}t}x(t) = \Lambda x(t)(1-x(t)) - x(t), \qquad x(0) = x_0, \tag{44}$$

which admits the general solution

$$x(t) = \left[\frac{1}{x_c} + \left(\frac{1}{x_0} - \frac{1}{x_c}\right)\mathrm{e}^{-(\Lambda-1)t}\right]^{-1}. \tag{45}$$

Along characteristics, the density satisfies

$$\frac{\mathrm{d}}{\mathrm{d}t}p(t) = \left[(2\Lambda + g)x(t) - (\Lambda - 1)\right]p(t), \qquad p(0) = p_0(x_0). \tag{46}$$

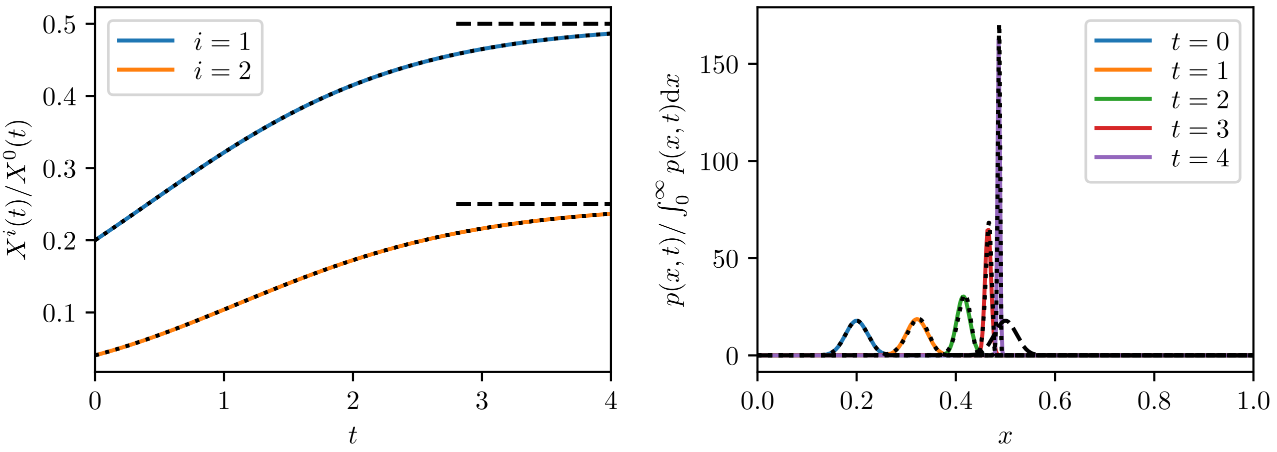

(a) $N = 3$, $\Omega = \infty$.

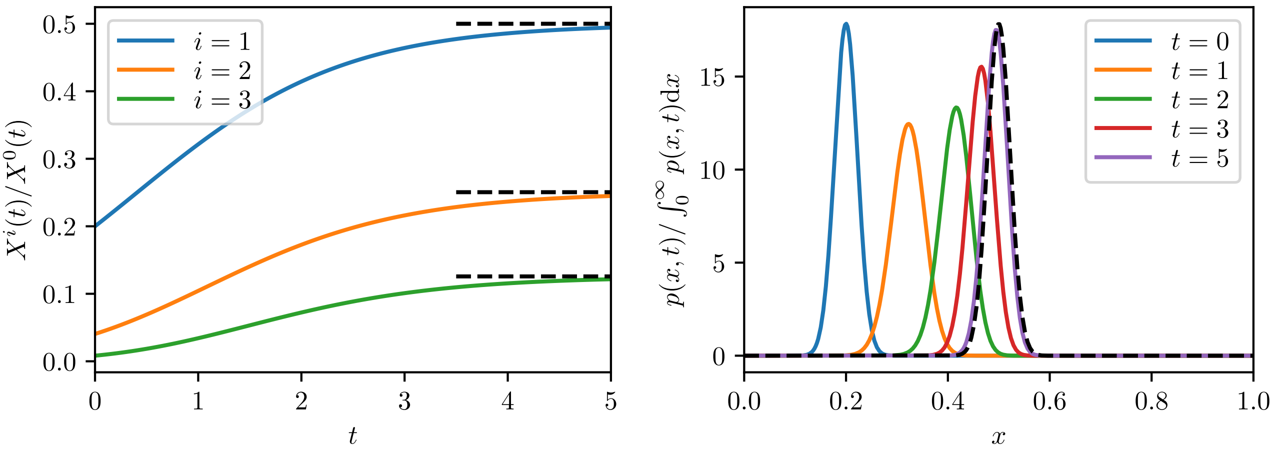

(b) $N = 4$, $\Omega = 1000$.

Figure 1: Normalised numerical solutions $X^i(t)$ of the moment equations (48) using the zero-information closure (coloured curves), compared to the moments of the long-time distribution (42) (black dashed curves), alongside the corresponding maximum-entropy distributions $p(x,t)$ at various times t (details in section 4). A truncation of N moments and different values of Ω are used. In (a) we set $\Omega = \infty$ and the black dotted curves depict the solution (45) and (47) of the first-order hyperbolic problem, while in (b) we set $\Omega = 1000$ and solve the parabolic problem. Other parameter values used were $\Lambda = 2$, $g = 1$, $p_0(x) = \mathrm{e}^{-1000(x-0.2)^2}\sqrt{1000/\pi}$.

Substituting the characteristic form of $x(t)$ from (45) and integrating, we find that the density satisfies

$$p(t) = p_0(x_0)\mathrm{e}^{-(\Lambda-1)t}\left[\frac{x_0}{x_c}\,\mathrm{e}^{(\Lambda-1)t} + 1 - \frac{x_0}{x_c}\right]^{2+g/\Lambda}. \tag{47}$$

Using the approach described in section 3, we determine that the associated moment hierarchy satisfies

$$\frac{\mathrm{d}}{\mathrm{d}t}X^i(t) = (g - i\Lambda)X^{i+1}(t) + i(\Lambda-1)X^i(t) + \frac{i(i-1)}{2\Omega}\left[(\Lambda+1)X^{i-1}(t) - \Lambda X^i(t)\right], \tag{48a}$$

$$X^i(0) = \int_0^\infty x^i p_0(x)\,\mathrm{d}x =: X_0^i. \tag{48b}$$

We emphasise that the only approximation made is that the distribution is not large at the boundary. Since the forms (40) are all polynomial, there is no other approximation, and thus any appreciable error in the moment equations (48) is the result of the moment closure.

We solve the system (48) numerically using an implicit BDF solver [8, 15, 46]. For the zero-information closure, we reconstruct the distributions corresponding to the solutions of the moment equations by finding the maximum-entropy distribution that shares the same first N moments (a component of the zero-information closure as described in section 4).

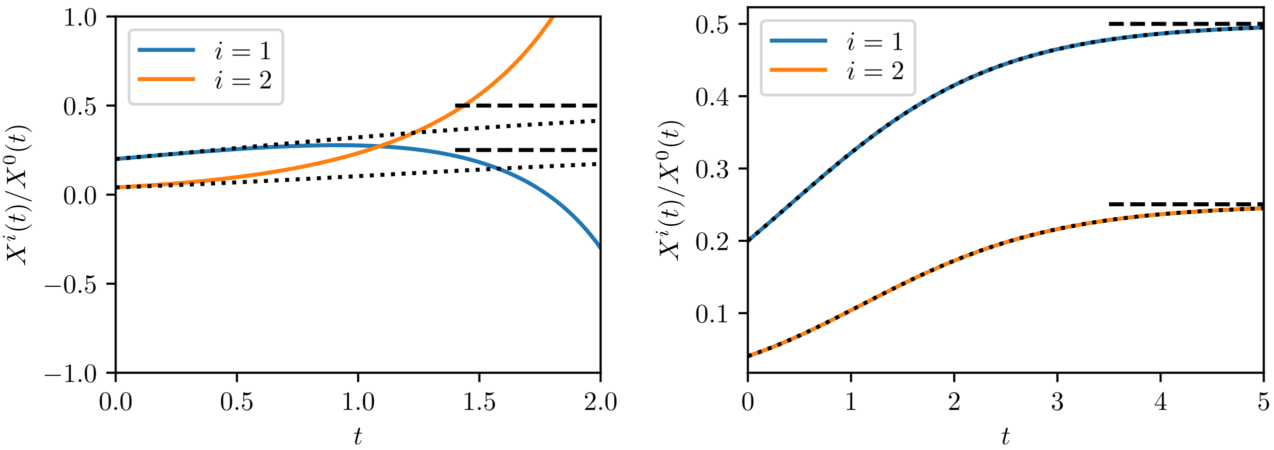

(a) Zero closure, $N = 3$.

(b) Central closure, $N = 3$.

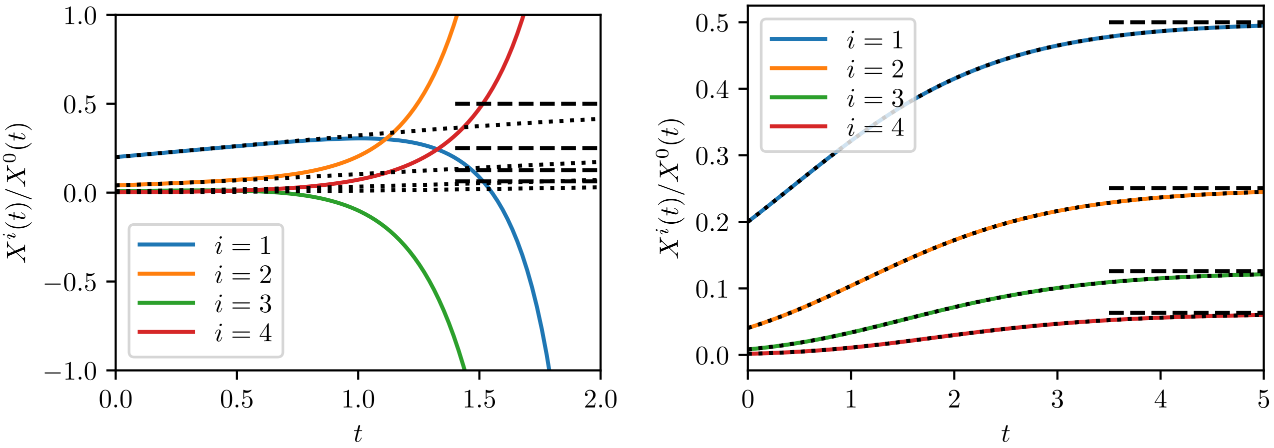

(c) Zero closure, $N = 5$.

(d) Central closure, $N = 5$.

Figure 2: Normalised numerical solutions $X^i(t)$ of the moment equations (48) using the zero and central closures (coloured curves), compared to the moments of the hyperbolic solution (45) and (47) (black dotted curves) and the moments of the long-time distribution (42) (black dashed lines). A truncation of N moments is employed along with parameters $\Omega = \infty$, $\Lambda = 2$, $g = 1$, and $p_0(x) = \mathrm{e}^{-1000(x-0.2)^2}\sqrt{1000/\pi}$.

In fig. 1a we solve the moment equations (48) in the limit $\Omega \to \infty$ by neglecting the term in square brackets. We find that the solution closely matches the solution of the hyperbolic PDE (43) (black dotted curves). This solution tends towards a Dirac mass at $x = x_c$, which has moments similar to the large-time solution (fig. 1a left) despite having noticeably different distributions (fig. 1a right, compare black dotted curve at $t = 4$ to black dashed curve). This discrepancy is precisely the result of neglecting the second-order noise term. When reinstated, the solution converges towards a distribution that demonstrates good agreement with the large-time solution (fig. 1b). We infer that, in this first example, the $\mathcal{O}(1/\Omega)$ contributions make a substantial difference in the distribution when solving the moment equations corresponding to the Fokker–Planck terms. We also mention, a posteriori, that the reconstructed distributions in fig. 1 are consistent with the assumption of negligible mass at the boundary.

The zero closure does not exhibit adequate performance. Moments quickly diverge and become negative (fig. 2a, note the time scale is shorter to zoom in on the divergent behaviour). Increasing the moment truncation order N appears to marginally delay the divergence but does not suppress it (fig. 2b). The central closure, on the other hand, seems to provide a good approximation (fig. 2c), which is robust to changes in the truncation order (fig. 2d). The plots in fig. 2 cover the limiting case of infinite system size Ω. Numerical examples illustrating essentially the same features for the case of finite Ω are available in the notebook of the code package published with this work. We proceed to study the moment equations and their closure for non-local terms.

6 Growth–fragmentation benchmarks

Having explored the behaviour of the Fokker–Planck dynamics using the moment equations, we now turn our attention to the non-local terms. We study two examples where again the reaction rates are of polynomial form, such that any error stems exclusively from the closure rather than the polynomial approximation. The growth–fragmentation benchmarks studied in Ref. [29] are of this form, with the additional benefit of admitting explicit solutions.

6.1 Cell division

In the first scenario we model a cell population in the copy-number paradigm. Each cell contains some initial copy number x of a static substance, that is, a substance that is no longer being produced but is also not decaying. Mother cells divide into two daughters with uniformly random copy numbers. The colony is housed in a bioreactor running in batch mode, and there are no other processes of relevance. The PDE takes the form

$$\frac{\partial}{\partial t}p(x,t) = -ax^k p(x,t) + \int_x^\infty 2ay^{k-1}p(y,t)\,\mathrm{d}y, \qquad p(x,0) = p_0(x). \tag{49}$$

The division rate is ax^k and the division kernel is self-similar and uniform: in the notation of section 2.1, $\theta_1(x \mid \hat{x}) = 1/\hat{x}$ for $x \in [0,\hat{x}]$ and $\Theta_1(y) = 1$ for $y \in [0,1]$.

Equation (49) admits the explicit self-similar solution [29]

$$\tilde{p}(x,t) = c\,(at)^{2/k}\mathrm{e}^{-atx^k}. \tag{50}$$

It will be helpful to also calculate the moments of solution (50),

$$\tilde{X}^i(t) := \int_0^\infty x^i \tilde{p}(x,t)\,\mathrm{d}x = c\,(at)^{(1-i)/k}\int_0^\infty x^i \mathrm{e}^{-x^k}\,\mathrm{d}x = \frac{c\,(at)^{(1-i)/k}}{k}\Gamma\left(\frac{i+1}{k}\right), \tag{51}$$

where Γ is the Gamma function. From the properties of the Gamma function, explicit expressions are available for $k = 1$ and $k = 2$.

For integer $k > 0$, the moment hierarchy associated with (49) is of the form

$$\frac{\mathrm{d}}{\mathrm{d}t}X^i(t) = a\left(\frac{1-i}{1+i}\right)X^{i+k}(t), \qquad X^i(0) = \int_0^\infty x^i p_0(x)\,\mathrm{d}x =: X_0^i. \tag{52}$$

Here again, since no approximations were made, these two moment hierarchies describe the exact evolution of the distribution's moments.

The self-similar solution (50) does not allow for an arbitrary initial condition, however, we expect that solutions for arbitrary initial conditions tend to the self-similar form in large time. We make some preliminary remarks without assuming the self-similar form. Since the distribution $p(x,t)$ must be non-negative, and assuming its continuity, we deduce that all moments are positive at time t if $p(x,t)$ is positive at some point $x \geq 0$. In this case, $X^i(t)$ is strictly decreasing for all $i > 1$ while $X^0(t)$ is increasing. The first moment $X^1(t)$ is time-invariant regardless of the other moments, as the fragmentation acts to increase the number of cells, but does not change the total copy number, leaving this a conserved quantity. It follows that the steady solution is a distribution whose ith moment is zero for all $i > 1$. The steady state cannot be reached in finite time: for any fixed $x > 0$, $p(x,t)$ decreases at most exponentially, therefore, the distribution remains positive for all time. From the self-similar solution (50) we may further observe that the ith moment is $\mathcal{O}(t^{(1-i)/k})$. In particular the zeroth moment diverges at a rate $\mathcal{O}(t^{1/k})$ while the moments $i > 1$ decay algebraically. Physically, all cells have divided infinitely to accumulate their mass at the $x = 0$ state.

What are the moment dynamics with a zero closure? The k highest-order moments, from order $N-k$ to order $N-1$, are time-invariant because the right-hand side of (52) vanishes in the closure. These moments thus retain their initial values. Assuming that these initial moments are positive, as must be the case physically, then the system cannot converge to the exact steady state. Fatally, the ith-order moment, for all $\max(2, N-2k) \leq i < \max(2, N-k)$, must decrease monotonically at a constant rate thus eventually becoming negative and tending to $-\infty$ whence it is no longer physically meaningful. We deduce that the ith-order moment, for all $\max(2, N-3k) \leq i < \max(2, N-2k)$, will eventually be monotonically increasing and diverge to ∞. This reasoning may be extended to all moments $i \geq 2$. We can only avoid this by setting the k highest moments to zero initially, which makes them vanish identically. However, the same reasoning may then be applied to the next k moments, and we find that the only way to avoid the diverging moments is to set all moments $i \geq 2$ to zero initially. The zero closure fails irreparably, and a more informed moment closure is required.

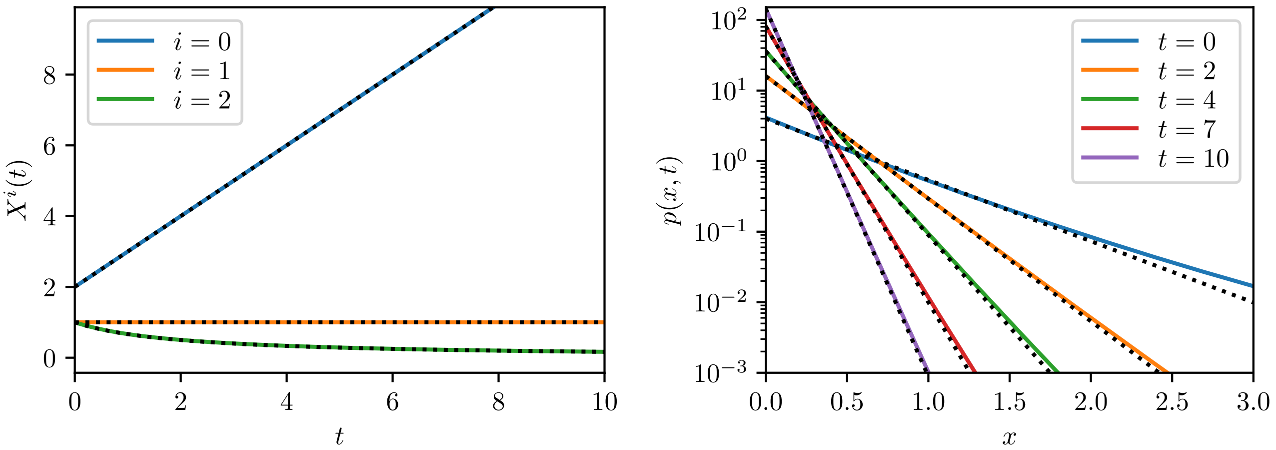

(a) $k = 1$.

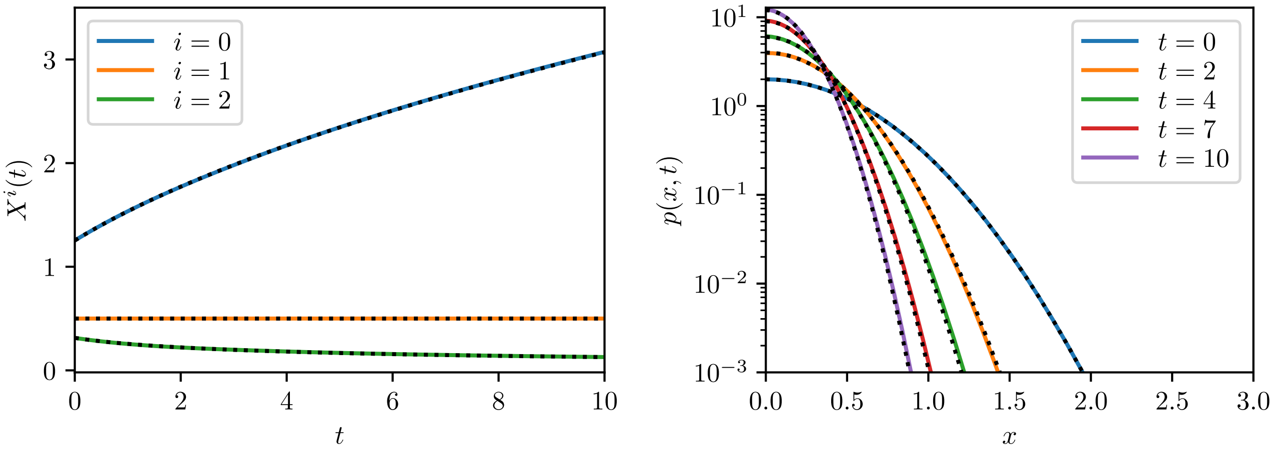

(b) $k = 2$.

Figure 3: Numerical solutions $X^i(t)$ of the moment equations (52) using the zero-information closure (coloured curves), compared to the moments of the self-similar solutions (51) (black curves), alongside the corresponding maximum-entropy distributions $p(x, t)$ at different times t (details in section 4) compared to the self-similar distribution given in (50). The initial condition is given by the self-similar solution at time $t = 2$: $p_0(x) = \tilde{p}(x, 2)$. The time parameter $a = 1$ is used with a truncation of $N = 3$ moments and different model parameters k.

We now study numerical solutions of the moment equations (52), which we again compute using an implicit BDF solver. The zero-information closure is capable of accurately reproducing the dynamics (fig. 3). We again reconstruct the underlying distributions by finding the distribution of maximum-entropy which shares its first N moments with the computed solution, as described in section 4. The distributions agree over several orders of magnitude (with some discrepancy in the tail of the initial distribution in fig. 3a right). We see in fig. 3 how the zeroth-order moment is increasing, while the first-order order moment remains constant, and the second order decreases, as described analytically above.

The zero closure exhibits divergent and non-physical behaviour (negative moments, as depicted in the notebook available in the code package published with this work). The central closure is not as good an approximation as we observed with the example in section 5, but it is also not wildly divergent (fig. 4). Increasing the truncation order can improve the agreement (figs. 4c and 4d) but does not always (figs. 4a and 4b).

6.2 Cell growth, cell division, and population dilution

We now move to a second scenario, in which we no longer consider the substance x to be static, and include a self-reinforcing production whose rate is equal to the copy number (per unit time). Moreover, we consider a random (discrete) transition that all cells can make irrespective of their internal state, say cell death, after which we no longer want to account for the substance. The growth rate in (3), the rate of cell division events, is $g_1(x) = akx^k$ (since we have just a single discrete state $\mathcal{K} = 1$). The division kernel in (3) is uniform, $\theta_1(x \mid \hat{x}) = 1/\hat{x}$, which, by (5), admits the self-similar representation $\Theta_1(y) = 1$ for $y \in [0, 1]$. Combining these ingredients, the PDE

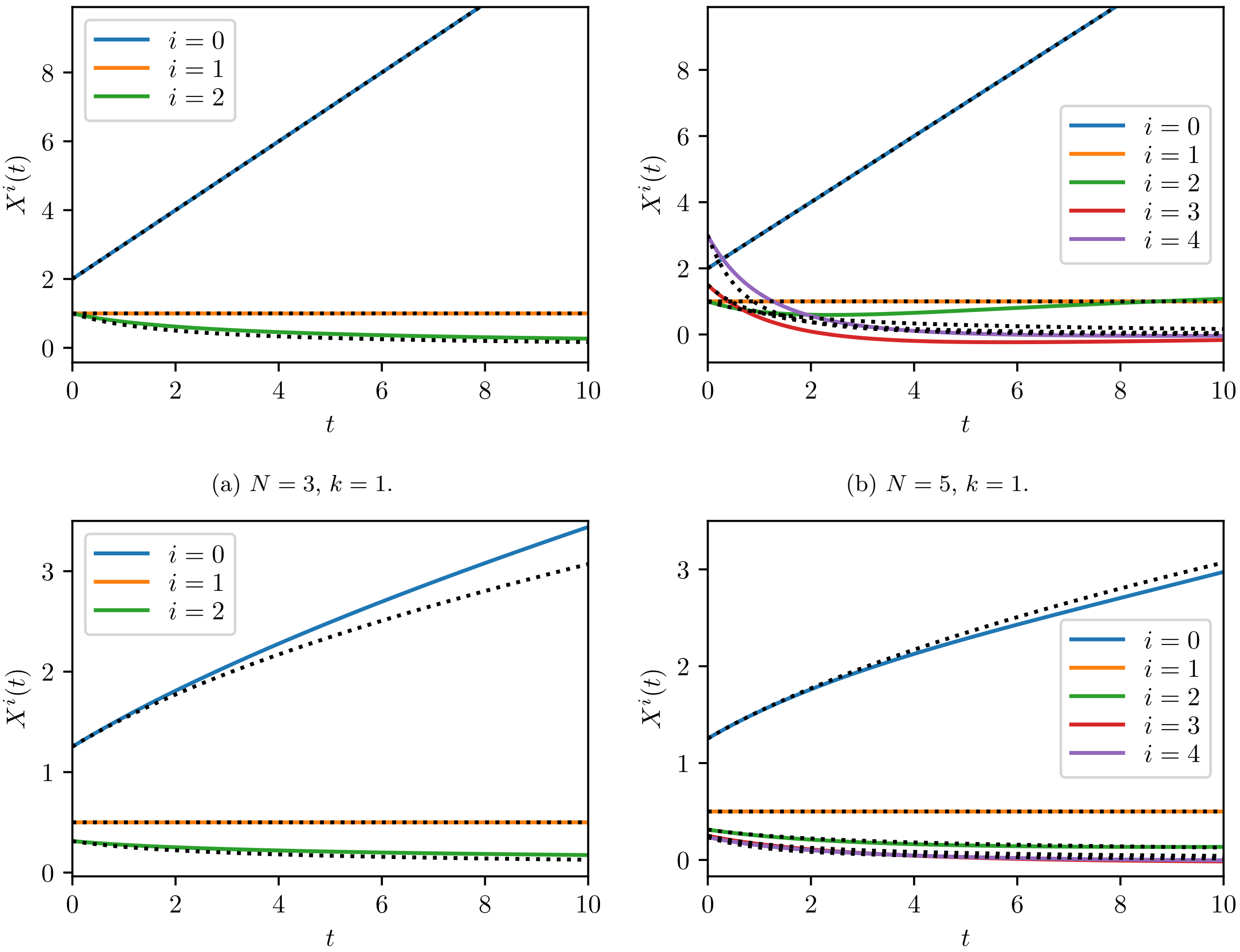

(a) $N=3$, $k=1$.

(b) $N=5$, $k=1$.

(c) $N=3$, $k=2$.

(d) $N=5$, $k=2$.

Figure 4: Numerical solutions $X^i(t)$ of growth–fragmentation model (52) using the central closure (coloured curves), compared to the self-similar solution (51). The initial condition is given by the moments of the self-similar solution at time $t=2$. The time parameter $a=1$ is used with different truncation orders N and model parameters k.

takes the form

$$\frac{\partial}{\partial t}p(x,t) = -\frac{\partial}{\partial x}\left[xp(x,t)\right] - (akx^k+1)p(x,t) + \int_x^\infty 2aky^{k-1}p(y,t)\,\mathrm{d}y, \qquad p(x,0)=p_0(x). \tag{53}$$

There is no second-order term associated with the production (as obtained in the deterministic limit $\Omega\to\infty$). The equation (53) admits the self-similar solution

$$\hat{p}(x,t) = c\left[a(1-\mathrm{e}^{-kt})\right]^{2/k}\mathrm{e}^{-a(1-\mathrm{e}^{-kt})x^k}. \tag{54}$$

Here too the moments may be calculated as follows:

$$\hat{X}^i(t) := \int_0^\infty x^i\hat{p}(x,t)\,\mathrm{d}x = c\left[a(1-\mathrm{e}^{-kt})\right]^{(1-i)/k}\int_0^\infty x^i\mathrm{e}^{-x^k}\,\mathrm{d}x = \frac{c\left[a(1-\mathrm{e}^{-kt})\right]^{(1-i)/k}}{k}\Gamma\left(\frac{i+1}{k}\right). \tag{55}$$

As opposed to the first model — where the dynamics are pure cell division, thus there is a diverging quantity of cells of increasingly small size — in this case, the production mechanism balances the copy-number loss due to cell division and the cell death balances the increasing cell count due to division, and the population tends to a non-singular distribution. For large time, $t\gg 1$, the distribution (53) has, up to exponentially small corrections, the limiting behaviour

$$\hat{p}(x,t) \sim c\,a^{2/k}\mathrm{e}^{-ax^k}, \tag{56}$$

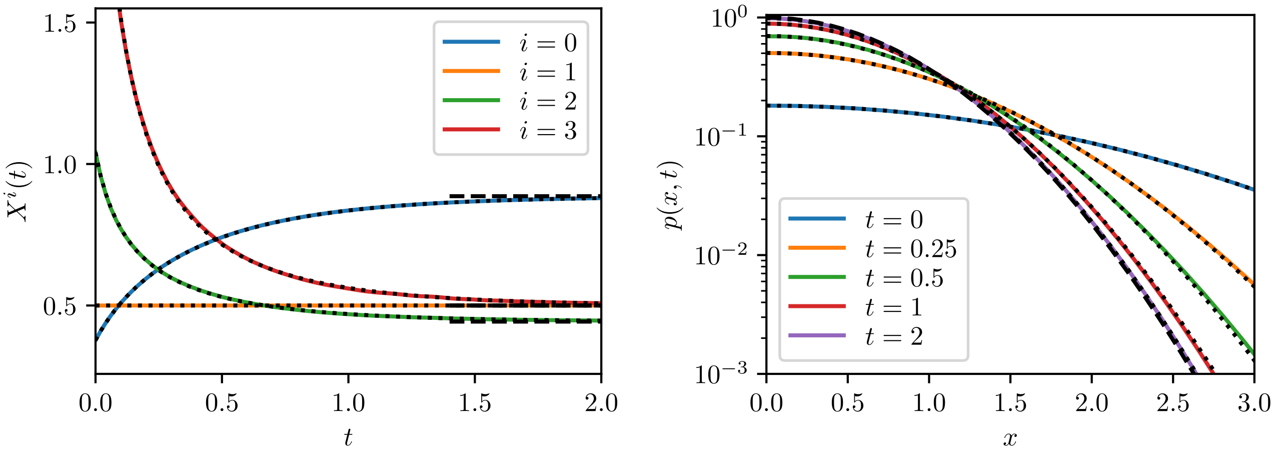

(a) $k = 2$.

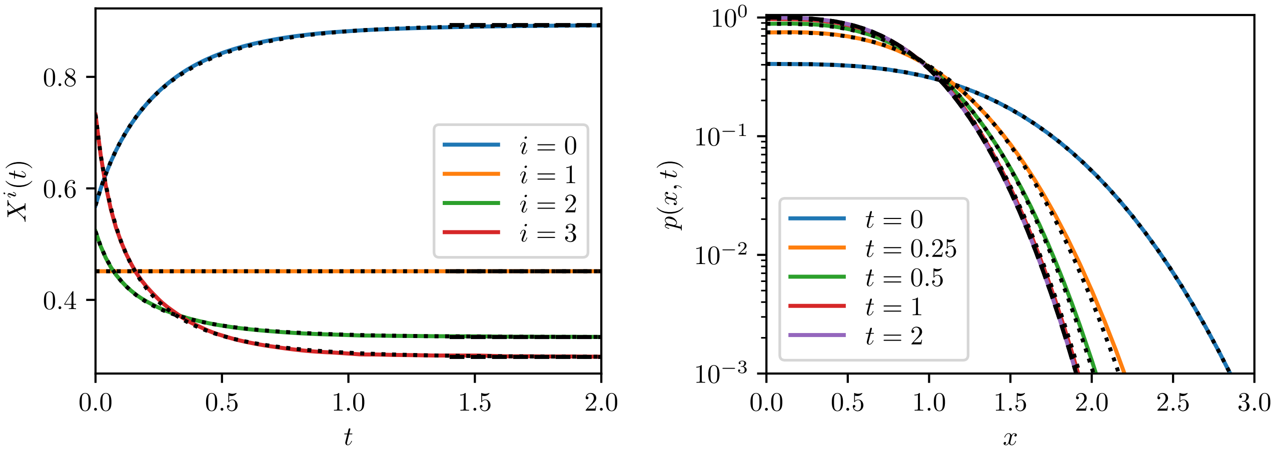

(b) $k = 3$.

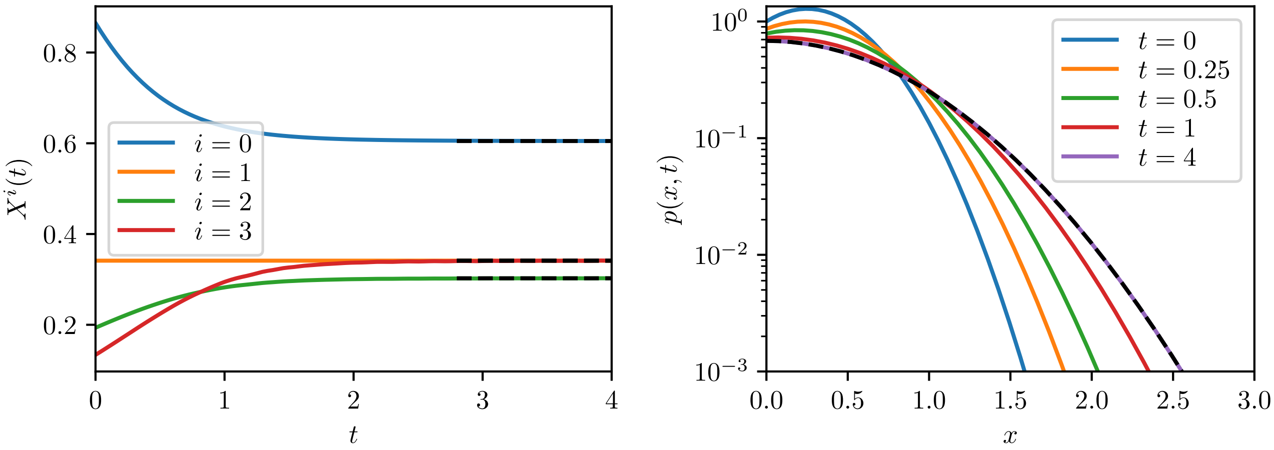

(c) $k = 2$.

Figure 5: Numerical solutions $X^i(t)$ of the moment equations (58) using the zero-information closure (coloured curves), compared to the self-similar solutions (55) (black dotted curves) and the large-time solution (57) (black dashed curves), alongside the corresponding maximum-entropy distributions $p(x,t)$ at different times t (details in section 4) compared with the self-similar distribution given in (54) with its large-time form in (56). The initial condition $p_0(x)$ is given by (a,b) the self-similar solution at time $t = 0.1$: $p_0(x) = \hat{p}(x, 0.1)$; (c) $p_0(x) = \mathrm{e}^{2x-4x^2}$. The time parameter $a = 1$ is used with truncation order $N = 4$ and different model parameters k.

and similarly the moments have the large-time behaviour

$$\hat{X}^i(t) \sim \frac{c\,a^{(1-i)/k}}{k}\Gamma\left(\frac{i+1}{k}\right). \tag{57}$$

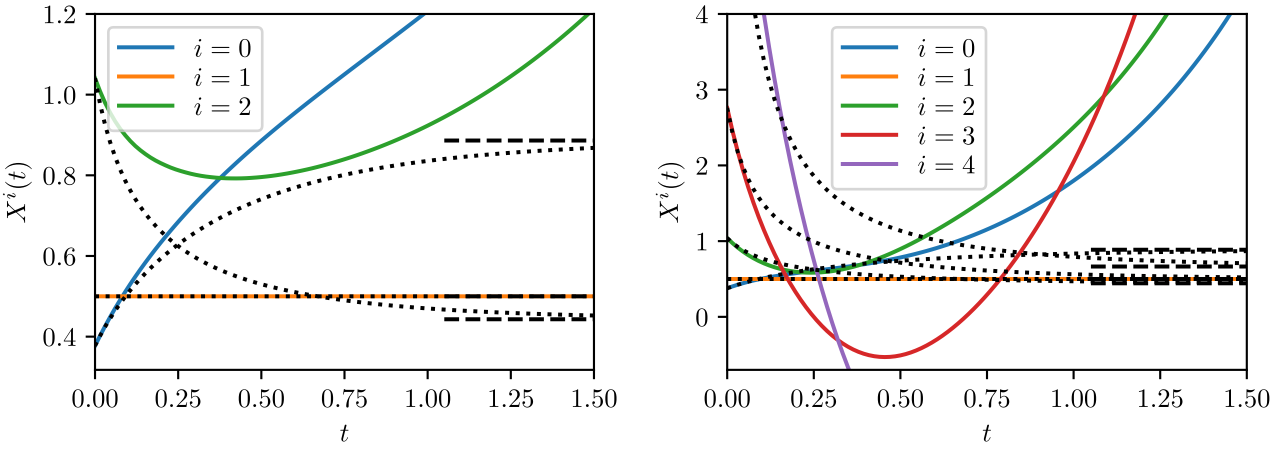

(a) $N=3$.

(b) $N=5$.

Figure 6: Numerical solutions $X^i(t)$ of growth–fragmentation model (52) using the central closure (coloured curves), compared to the self-similar solution (55) (black dotted curves), and the large-time solution (57) (black dashed lines). The initial condition is given by the moments of the self-similar solution at time $t=0.1$. Parameters $a=1$ and $k=2$ are used with different truncation orders N.

For integer $k>0$, the moment hierarchy corresponding to (53) is

$$\frac{\mathrm{d}}{\mathrm{d}t}X^i(t) = (i-1)X^i(t) + ak\left(\frac{1-i}{1+i}\right)X^{i+k}(t), \qquad X^i(0) = \int_0^\infty p_0(x)\,\mathrm{d}x =: X_0^i. \tag{58}$$

The hierarchy (58) admits steady solutions that satisfy the recurrence relation

$$X^i = \frac{ak}{1+i}X^{i+k}, \tag{59}$$

for all $i \neq 1$, where X^1 is constant for all t and thus retains its initial value. It may be verified directly that the large-time solution (57) satisfies the recurrence relation (59).

For this growth–fragmentation example, we see that the zero closure leaves the moments $X^i(t)$ growing exponentially for $i \geq \max(2, N-k)$ and for all time. This disagrees with the finite steady-state moments (57). More fatally, this closure leads to (non-physical) negative moments. To see this, note that for all i such that $\max(2, N-k) \leq i < N$, the ith moment is an exponential with growth rate $i-1$. Then, for all i such that $\max(2+k, N-k) \leq i+k < N$, the ith moment satisfies an ODE of the form $\dot{x}(t) = (i-1)x(t) - c\,\mathrm{e}^{(i+k-1)t}$ for some $c>0$, whose solution is of the form $x(t) = d\mathrm{e}^{(i-1)t} - c\,\mathrm{e}^{(i+k-1)t}/k$ for some constant d. Therefore, for large enough time, the solution behaves like $-\mathrm{e}^{(i+k-1)t}$, diverging to $-\infty$. This reasoning may be repeated for moments i, where $\max(2+2k, N-k) \leq i+2k < N$, who will eventually behave as $\mathrm{e}^{(i+k-1)t}$. We may continue in this manner for all moments beyond first order to demonstrate that they will diverge. We deduce that the structure neglected in the zero closure leaves a non-physical moment system, which is confirmed by numerical simulations (examples available in the notebook of the code package published with this work).

The zero-information closure is capable of accurately approximating the system, demonstrating agreement over several orders of magnitude (fig. 5). For an initial condition of self-similar form, the moment-closure solution (coloured curves) aligns with the self-similar solutions (black dotted curves, figs. 5a and 5b). For an initial condition not of self-similar form, we observe rapid convergence to the large-time self-similar solution (56) (black dashed curves, fig. 5c). Note how the zeroth-order self-similar moment $\hat{X}^0(t)$ in (55) is increasing while moments of order two and above are decreasing (as demonstrated in figs. 5a and 5b). For the non-self-similar example we chose the zeroth-order moment above its steady-state value and the higher-order moments below the steady-state value, such that the moment dynamics are qualitatively different from the self-similar case.

On the other hand, numerical solution using the central closure exhibits divergent behaviour (fig. 6a). Increasing the truncation order reveals that this closure too suffers from non-physical negative moments (fig. 6b). Note the time scale in fig. 6 is significantly shorter than for the zero-information closure in fig. 5 due to the divergence.

We conclude that both the naive zero closure as well as the central closure are not always feasible strategies. This observation is already well established in the biochemical literature for discrete master equations, for example, spurious dynamics including non-physical states where moments become negative have been studied in Refs. [37, 43, 44, 47]. However, we reiterate its relevance in the case of the present class of continuum population models.

Moreover, we stress that the cell-division explored here is a population-level process that extends beyond the realm of the master equation [29], and thus the observation is extended to an altogether new class of processes. We further note that implementing the zero-information closure in the continuum (rather than a discrete state space, as was done in the original paper Ref. [48]) introduces new sources of error, as sums are replaced by integrals, which must be approximated via numerical quadrature.

With this in mind, it might be tempting to think that optimising high-order moment systems is a task doomed to failure: naive closures are typically expected to fail, and sophisticated closures, such as the zero-information closure, are difficult to implement in an optimisation framework and prohibitively costly. The primary motivation for introducing a moment approximation and closure is to avoid optimising the original heterogeneous model. However, if the reduced-order system is similarly intractable, then we have not achieved any improvement. It is for this reason that the result in the following section is both useful and unexpected.

7 Controlling a microbial consortium

Microbial consortia are colonies of two or more interacting microorganisms living together. Such colonies offer increased application potential over cultures of single strains since each organism can be specialised for different tasks, allowing a diverse set of mechanisms that need not coexist in a single organism. This promises improvements in bioproduction, bioremediation, and other areas [6, 25, 41, 58].

7.1 A microbial consortium model

In this section we study a model of a microbial consortium (from Ref. [31]), where two strains are maintained within a single bioreactor with the aim of producing a protein of interest (denoted by the state y). We consider a construct in which a photoreceptive transcription factor (TF) is constitutively produced. Upon light induction, the TF (denoted by the state x) is recruited in the production of recombinase which leads to recombination. Only in the recombined cell construct is the protein of interest produced. The light induction leads to a community of two genetically distinct subpopulations. We assume that the original (unrecombined) cells grow at some rate A, while the recombined cells have an inhibited growth rate $0 \leq a(y) < A$, due to the presence of the protein, which is toxic to the cell. In fact, in such cases, microbial consortia are considered particularly useful, since a healthy and growing subpopulation can be maintained alongside the subpopulation that is effectively poisoning itself to produce the protein of interest, thereby retaining both a growing population and protein production [41]. We thus call the original (unrecombined) cells the “growers” and the recombined cells the “producers”. We further assume that the TF recruitment and cell recombination is faster than the other transient timescales and may be neglected.

The inhibited growth rate should satisfy $a(0) = A$ and $a(\infty) = a_\infty \in [0, A)$. We consider the monotonically decreasing Hill form

$$a(y) = a_\infty + \frac{A - a_\infty}{1 + (y/L)^m}, \tag{60}$$

where the growth rate $a(y) \in [a_\infty, A]$ interpolates nonlinearly between the minimum and maximum growth rates, a_∞ and A, respectively, and the characteristic protein concentration associated with diminished growth is denoted L.

The recombination is modulated by the level of TF via $h(x)$ which takes the Hill form

$$h(x) = \frac{x^n}{K^n + x^n}, \tag{61}$$

for a characteristic concentration K and a Hill coefficient n.

The governing PDE takes the form

$$\frac{\partial}{\partial t} g(x,t) = A g(x,t) - \Lambda(t) g(x,t) - f u(t) h(x) g(x,t) - \frac{\partial}{\partial x}[(\alpha - \beta x) g(x,t)] + \frac{1}{2\Omega}\frac{\partial^2}{\partial x^2}[(\alpha + \beta x) g(x,t)], \tag{62a}$$

$$\frac{\partial}{\partial t} p(y,t) = a(y) p(y,t) - \Lambda(t) p(y,t) - \frac{\partial}{\partial y}[(\mu - \nu y) p(y,t)] + \frac{1}{2\Omega}\frac{\partial^2}{\partial y^2}[(\mu + \nu y) p(y,t)], \tag{62b}$$

for a maximal recombination rate f, subject to the boundary conditions

$$(\alpha - \beta x) g(x,t) - \frac{1}{2\Omega}\frac{\partial}{\partial x}[(\alpha + \beta x) g(x,t)] = 0, \qquad \text{at } x = 0 \text{ and as } x \to \infty, \tag{62c}$$

$$(\mu - \nu x) p(y,t) - \frac{1}{2\Omega}\frac{\partial}{\partial y}[(\mu + \nu x) p(y,t)] = \begin{cases} f u(t) \int_0^\infty h(x) g(x,t)\,\mathrm{d}x, & \text{at } y = 0, \\ 0, & \text{as } y \to \infty. \end{cases} \tag{62d}$$

The turbidostat dilution rate is

$$\Lambda(t) = A\int_0^\infty g(x,t)\,\mathrm{d}x + \int_0^\infty a(y)p(y,t)\,\mathrm{d}y. \tag{62e}$$

We impose the initial conditions

$$g(x,0) = g_0(x), \qquad\qquad p(0) = 0, \tag{62f}$$

where $g_0(x)$ is the stationary solution of (62a) with no light input $u(t) = 0$. This choice reproduces typical lab conditions where the optogenetic strains are cultivated in the dark for several cell generations.

We seek to maximise total production of the protein of interest, given by

$$J_{\mathrm{PDE}} = \int_0^\infty yp(y,T)\,\mathrm{d}y + \int_0^T \Lambda(t)\int_0^\infty yp(y,t)\,\mathrm{d}y\,\mathrm{d}t. \tag{62g}$$

Using the shorthands

$$X^i(t) := \int_0^\infty x^i g(x,t)\,\mathrm{d}x, \qquad\qquad Y^i(t) := \int_0^\infty y^i p(y,t)\,\mathrm{d}y, \tag{63}$$

and assuming that the functions $h(x)$ and $a(y)$ have polynomial approximations

$$h(x) \approx \sum_{j=0}^{N(h)} h_j x^j, \qquad\qquad a(y) \approx \sum_{j=0}^{N(a)} a_j y^j, \tag{64}$$

we use the components derived in section 3 to obtain the moment hierarchy approximation

$$\begin{aligned}\dot{X}^i(t) &= (A-\Lambda(t))X^i(t) - fu(t)\sum_{j=0}^{N(h)} h_j X^{j+i}(t)\\ &\quad + i(\alpha X^{i-1}(t) - \beta X^i(t)) + \frac{i(i-1)}{2\Omega}(\alpha X^{i-2}(t) + \beta X^{i-1}(t)), &&\text{(65a)}\\ X^i(0) &= \left(\frac{\alpha}{\beta}\right)^i + \mathcal{O}(\Omega^{-1}), &&\text{(65b)}\\ \dot{Y}^i(t) &= \sum_{j=0}^{N(a)} a_j Y^{j+i}(t) - \Lambda(t)Y^i(t) + \delta_{i0}fu(t)\sum_{j=0}^{N(h)} h_j X^j(t)\\ &\quad + i(\mu Y^{i-1}(t) - \nu Y^i(t)) + \frac{i(i-1)}{2\Omega}(\mu Y^{i-2}(t) + \nu Y^{i-1}(t)), &&\text{(65c)}\\ Y^i(0) &= 0, &&\text{(65d)}\end{aligned}$$

for

$$\Lambda(t) = AX^0(t) + \sum_{j=0}^{N(a)} a_j Y^j(t), \tag{65e}$$

where δ_{i0} is the Kronecker Delta function, that takes the value one when $i = 0$ and zero otherwise. For $i = 0, 1$, we understand that terms in equations (65a) and (65c) with a zero coefficient vanish (so no negative indices are encountered). In other words,

$$\begin{aligned}\dot{X}^0(t) &= (A-\Lambda(t))X^0(t) - fu(t)\sum_{j=0}^{N(h)} h_j X^j(t), && X^0(0) = 1, &&\text{(65f)}\\ \dot{X}^1(t) &= (A-\Lambda(t))X^1(t) - fu(t)\sum_{j=0}^{N(h)} h_j X^{j+1}(t) + (\alpha X^0(t) - \beta X^1(t)), && X^1(0) = \frac{\alpha}{\beta}, &&\text{(65g)}\end{aligned}$$

and similarly for $\dot{Y}^0(t)$ and $\dot{Y}^1(t)$.

We seek to maximise the objective

$$J_{\mathrm{MC}} = Y^1(T) + \int_0^T \Lambda(t)Y^1(t)\,\mathrm{d}t. \tag{65h}$$

The initial conditions in (65) may be determined consistently by seeking the stationary solution when $u(t) = 0$ and $Y^i(0) = 0$. We note that $Y^i(t) = 0$ for all time t, therefore, $\Lambda = AX^0$, and, for $i = 0$, we have $A(1-X^0)X^0 = 0$. In light of the conservation law $X^0(t) + Y^0(t) = 1$, it follows that $X^0 = 1$. For $i = 1$, we find that $X^1 = \alpha/\beta$. For $i \geq 2$ we derive the recurrence relation

$$X^i = \frac{\alpha}{\beta}\left(1 + \frac{i-1}{2\Omega}\right)X^{i-1} + \frac{\alpha}{\beta}\frac{i-1}{2\Omega}X^{i-2}. \tag{66}$$

In the limit as $\Omega \to \infty$, the leading-order solution is given by $X^i = (\alpha/\beta)^i$.

7.2 Influence of heterogeneity

Before proceeding to discuss the technical aspects of function expansion and approximations of the propensities, we highlight a general analytical result. Applying the quotient rule, and then using (65f) and (65g), we find that the mean protein level obeys the dynamics

$$\begin{aligned}\frac{\mathrm{d}}{\mathrm{d}t}\left(\frac{X^1(t)}{X^0(t)}\right) &= \frac{X^1(t)}{X^0(t)}\left(\frac{\dot{X}^1(t)}{X^1(t)} - \frac{\dot{X}^0(t)}{X^0(t)}\right)\\ &= \alpha - \beta\frac{X^1(t)}{X^0(t)} \underbrace{- fu(t)\sum_{j=0}^{N(h)} h_j \frac{X^1(t)}{X^0(t)}\left(\frac{X^{j+1}}{X^1(t)} - \frac{X^j(t)}{X^0(t)}\right)}_{\text{Heterogeneous contribution}}, \qquad (67a)\end{aligned}$$

$$\frac{X^1(0)}{X^0(0)} = \frac{\alpha}{\beta}. \tag{67b}$$

There are contributions to the mean dynamics that go beyond the commonly used homogeneous birth–death model (see, e.g., Ref. [31]). These come from the higher-order moments when $u(t) > 0$ and reflect the heterogeneity of the distribution that, upon light induction, acts to bias the distribution due to state-dependent recombination. In fact, we see that the first term in the sum, for $j = 0$, vanishes. This reflects the fact that, if $h(x) = h_0$ is constant, the recombination is not state-dependent and thus there is no additional contribution to the mean dynamics. Neglecting this heterogeneity can result in unsatisfactory controls [31].

It might be tempting to think that the linear-noise approximation (LNA) [36, Ch. 6] could provide us with a heterogeneity-aware approximation of the PDE system. However, one must keep in mind that the LNA yields a leading-order system equivalent to the reaction-rate equations [55], which is exactly the homogeneous approximation mentioned above [31]. The first-order perturbation capturing the heterogeneous fluctuations due to noise do not influence the leading-order system, and thus do not enter the control problem formulation at leading order, in contrast to (67).

7.3 Function expansions and approximations

In this section, we use the concrete example introduced in section 7.1 as the basis to compare alternative approximation approaches. Ultimately, we find that, for this case study, the approach taken in this work has important practical advantages.

7.3.1 Rational function hierarchies

In deriving the moment hierarchy, we assumed a polynomial approximation of the non-polynomial functions $a(y)$ and $h(x)$ defined in (60) and (61). In the present example, the functions $a(y)$ and $h(x)$ are, up to addition or multiplication by a constant, of Hill form: $\xi^n/(K^n + \xi^n)$. The Hill functional form is rational assuming $n \in \mathbb{N}$, in that it is the ratio of two polynomial forms. In Ref. [35] it is shown that a moment hierarchy may be derived without the need for polynomial approximation by multiplying the governing equations by the denominators of all rational functions before multiplying by x^i and integrating.

Avoiding the need for approximation is appealing, however, this approach suffers several major drawbacks. First, it is inapplicable if the nonlinear propensity is not rational, as would be the case for non-integer n. Second, the resulting moment equations obtain a coupling of the ith moment to the $(i+n)$th moment. For large (integer) n, such as the example we use from the literature where $n = 10$, to resolve the $i = 0$ moment requires accurate resolution of the $i + n = 10$ moment. This high-order coupling can require the accurate resolution of an infeasibly large number of moments.

Third, for integer n, it is still not directly applicable to the example at hand. To see this, note that, even when multiplying (62a) and (62b) by the denominators of $h(x)$ and $a(y)$, the inhomogeneous boundary condition (62d), describing the recombination from grower to producer, remains with the rational form $h(x)$. This can be remedied by recasting the PDE in the full state space where both growers, $g(x, y, t)$, and producers, $p(x, y, t)$, are distributed over the full (x, y)-state space. The initial conditions (62f) are extended to $g(x, y, 0) = g_0(x)\delta(y)$ for the Dirac delta function and $p(x, y, 0) = 0$ remains. The boundary conditions (62c) and (62d) become zero normal flux in both dimensions for each variable. Crucially, the inhomogeneous term from the boundary condition (62d) becomes a bulk term in the PDE. Integrals in the dilution rate (62e) and the objective (62g) must be extended over the entire state space. This reformulation allows the nonlinearity at the boundary to be placed in the bulk and the approach is restored. Nevertheless, the cost is that the moment hierarchy returns to two dimensions, and we must now multiply the equation for p by both denominators of $h(x)$ and $a(y)$. Thus, returning to the second point, the $\boldsymbol{i} = (0, 0)$ moment will be coupled to the $\boldsymbol{i} = (n, m)$ moment. In our example, this is of degree $n + m = 20$, and we see that for system dimension larger than one the problem is exacerbated. The requisite system size is not smaller than a feasible discretisation of the full PDE model.

In a related work [21] rational propensities are preserved by formulating the moment hierarchy for *rational* moments. This avoids the final problem mentioned above: the boundary condition retains its rational form, which may be expressed as a combination of *rational* moments. While this circumvents the need to repose the problem on the full state space, and thereby sidesteps mixed moments of exceedingly high degree, it retains the first two drawbacks. The high-order coupling comes from having to express the regular moments obtained from the time-derivatives in terms of rational moments. This is a problem that does not present itself in the original work, as the authors study only steady states. However, in our setting, this induces the same order coupling discussed earlier.

We note that combining the above techniques with a low-degree rational approximation — either by reducing the Hill coefficient n or seeking a low-degree Padé approximant for general nonlinear functions — might be a viable approach. Nevertheless, for the aforementioned reasons, we do not pursue this technique here any further and instead we turn our attention to polynomial approximation of the nonlinear propensities.

7.3.2 Taylor expansions

Perhaps the first thing that comes to mind is a truncated Taylor expansion of a function around a given point. Despite being real analytic for $n \in \mathbb{N}$ (the function is not analytic at zero for non-integer n), these functions have complex singularities on the circle of radius K, since the denominator vanishes at $\xi = -K\zeta$ for any $\zeta^n = -1$ which is of unit modulus. Therefore, the radius of convergence of any power series will be limited by how close the singularities are to the expansion point. We see this graphically in fig. 7a, where we need to expand around several different points to approximate the Hill function on the domain $[0, 1]$. There is wild deviation from the Hill function at distances of more than approximately 0.1 from the expansion point. We infer that a fixed Taylor series will not provide a sufficiently accurate polynomial approximation.

A related method studied in the literature extends this idea by not taking a single fixed expansion point, but rather expanding around the mean of the distribution [2, 5, 13, 19, 22, 24]. The appeal of this approach is that, for distributions concentrated around their mean, the truncated Taylor expansion should constitute a close polynomial approximation of the Hill function. This approach may be implemented by representing the Taylor expansion in a power series form by using the binomial theorem

$$h(x) \approx \sum_{j=0}^{N(h)} \frac{1}{j!} h^{(j)} \left(\frac{X^1(t)}{X^0(t)} \right) \left(x - \frac{X^1(t)}{X^0(t)} \right)^j =: \sum_{j=0}^{N(h)} h_j x^j. \tag{68}$$

This proved to be numerically unstable for all approximation degrees $N(h)$, possibly owing to the large polynomial coefficients h_j.

To avoid having to translate the Taylor expansion form into a power series representation, we reformulate the moment hierarchy in terms of central moments, as described in full in Appendix C. This is achieved by defining moments centred at the distribution mean, and deriving the associated central moment equations. This formulation produced acceptable forward simulation results for sufficiently low Taylor truncation order, however, we were unable to obtain convergent results for the optimal control problem.

The truncated Taylor approximation at a fixed point is only locally accurate. While this motivated expanding at the mean, perhaps part of the difficulty in obtaining convergent optimisation results is due to the fact that the polynomial approximations are not “stationary”. These two potential shortcomings motivate the consideration of “stationary” polynomial approximations that are accurate over a sufficiently large region of the state space (of course, polynomial approximations diverge, and thus can not accurately approximate bounded functions, for example, over the entire state space).

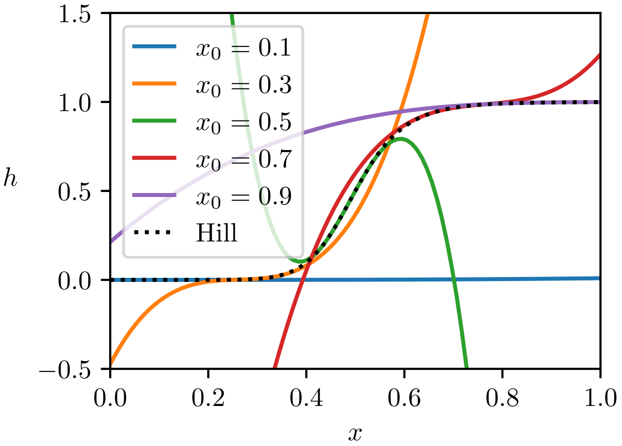

(a)

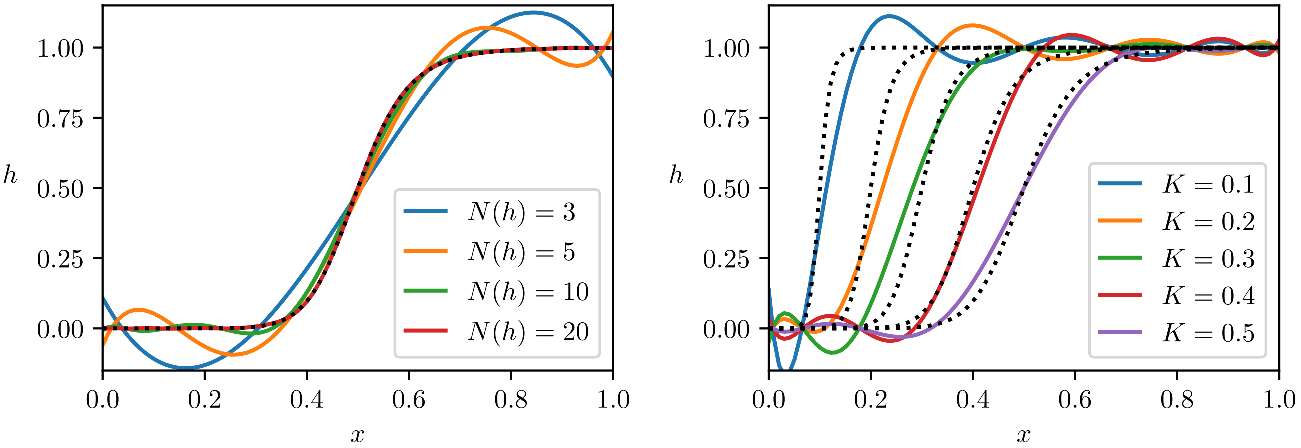

(b) $K = 0.5$.

(c) $N(h) = 8$.

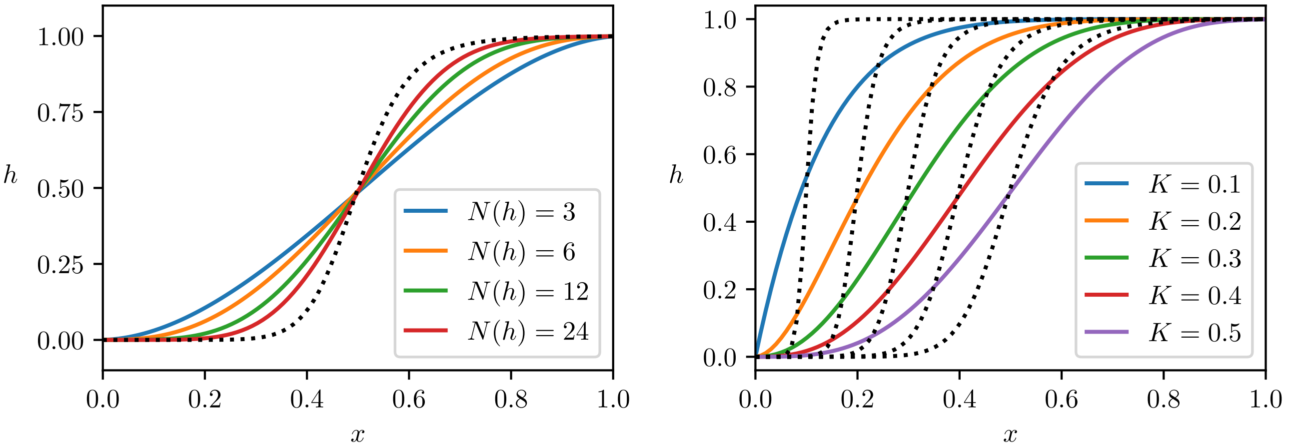

(d) $K = 0.5$.

(e) $N(h) = 8$.

Figure 7: (a) Series expansions of the Hill function $h(x)$ in (61) for $n = 10$ and $K = 0.5$ around different points $x = x_0$ for $N(h) = 3$. (b,c) Chebyshev interpolants for different degrees $N(h)$ and Hill parameters K. (d,e) Bernstein approximants for different degrees $N(h)$ and Hill parameters K.

7.3.3 Polynomial approximants

Given a closed interval, which we take to be $[0, 1]$, without loss of generality, and a polynomial degree $N(h)$, there exists a polynomial that best approximates the Hill function (in the L^∞ sense). Minimax algorithm, such as Remez's algorithm, may be used to determine such a polynomial. A close approximation of the optimal

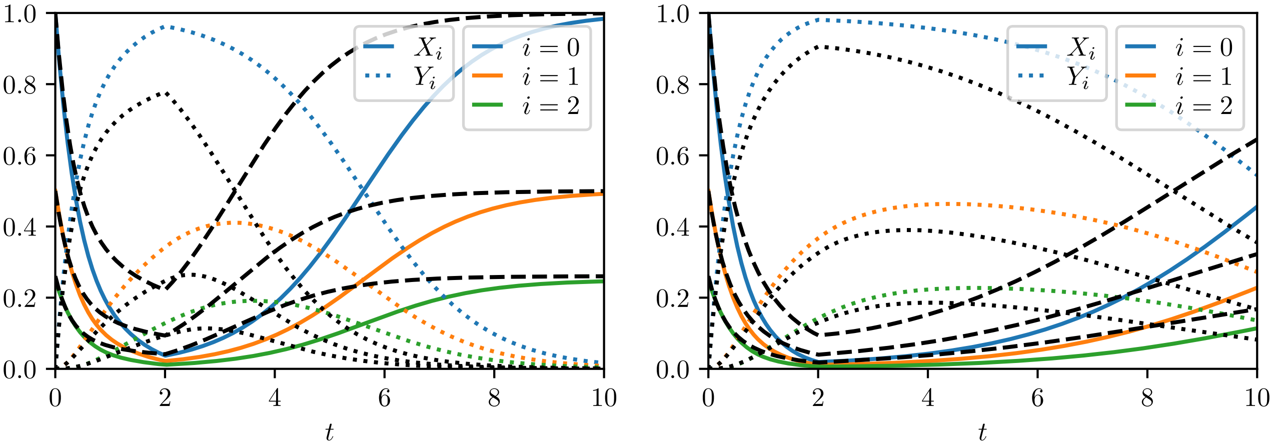

(a) $L = 0.1$.

(b) $L = 0.5$.

Figure 8: Moments of the full distribution (black curves) governed by (62) (solved using the discretisation from Ref. [31]) compared to solution of the moment equations (coloured curves) governed by (65) and using Bernstein approximants with $N(h) = N(a) = 3$ and a zero moment closure for $N = 15$ moments. The black dashed curves correspond to moments $X^i(t)$ while the black dotted curves correspond to $Y^i(t)$. The light profile (70) was employed, for various Hill parameters L and the default parameters in (69).

polynomial is the Chebyshev series that interpolates the function at the Chebyshev points of the first kind. This approximation converges to the optimal approximation as the degree tends to infinity. For extended discussion and demonstration of these points, we refer the reader to Ref. [53]. Indeed, for the Hill function, we see that the convergence is rapid (fig. 7b). Nevertheless, for degree $N(h) = 8$, the approximations when varying the Hill parameter K show large oscillations (fig. 7c; this is not Runge's phenomenon, since the sampling points are not equispaced). The magnitude of these oscillations, and the fact that the approximation can change sign when the original function cannot, renders them practically challenging.

To remedy this, we turn to Bernstein polynomials [10, Ch. 6], which can provide a constructive proof of Weierstrass' theorem and exhibit favourable analytical properties. In particular, the Bernstein approximants of a function converge to the function *and its derivatives*. Moreover, the approximant lies between the function's extrema and its derivatives are uniformly bounded in proportion to the function's derivatives. Approximants preserve monotonicity and convexity. These properties demonstrate how the approximant mimics important features of the original function structure. In particular, it will not suffer from the oscillations and sign changes of its Chebyshev counterpart. However [10], "There is a price that must be paid for these beautiful approximation properties: the convergence of Bernstein polynomials is very slow", as illustrated in fig. 7d. Nevertheless, for various values of K, the approximants preserve the qualitative features of the Hill function (fig. 7e).

Before presenting numerical results, we mention that, in addition to polynomials, there are other bases that may be used to form closed moment hierarchies, such as algebraic-trigonometric polynomials [23]. Nevertheless, polynomial forms are particularly useful in the biosciences because several propensities are naturally of polynomial form (e.g. mass-action kinetics and enzyme kinetics). Moreover, finite-dimensional approximation in such a basis could introduce oscillations, which, just as for the Chebyshev polynomials, are liable to creating undesirable local minima in the objective landscape.

7.4 Numerical Results

In all of the numerical simulations in this section, we use the default parameter values

$$N(a) = N(h) = 4, \quad A = 1, \quad a_\infty = 0, \quad f = 4, \quad m = n = 10, \quad K = 0.5, \quad \alpha = 0.5, \quad \beta = 1, \quad \mu = 0.5, \quad \nu = 1. \tag{69}$$

First, in fig. 8, we illustrate the moments of the forward problem solved when applying the light control profile

$$u(t) = \begin{cases} 1, & t \leq 2, \\ 0, & t > 2. \end{cases} \tag{70}$$

The comparison shows that the moments of the full distribution (coloured curves) are somewhat different from the moments obtained by solving the moment equations (65) using Bernstein approximants with $N(h) = N(a) = 3$ and

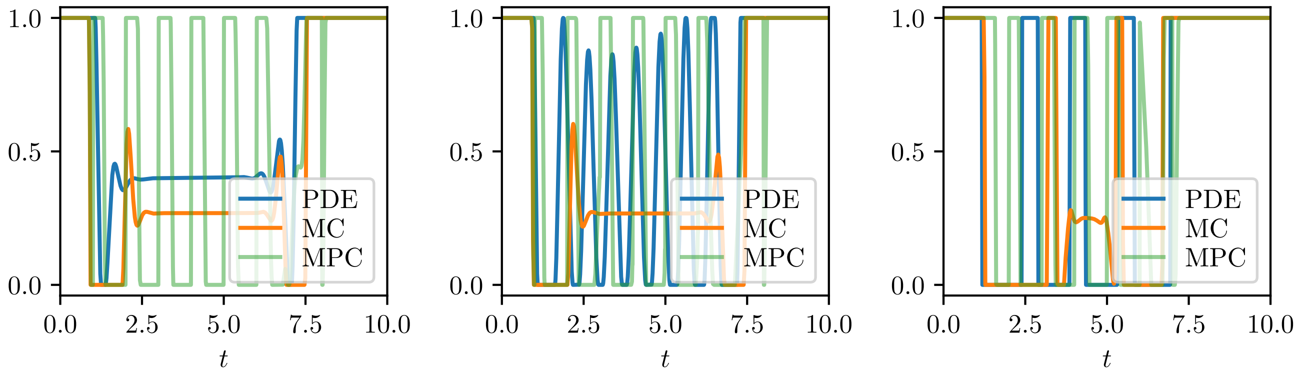

(a) $L = 0.1$: $\begin{pmatrix}\mathcal{J}_{\mathrm{MC}}\\ \mathcal{J}_{\mathrm{MPC}}\end{pmatrix} = \begin{pmatrix}0.952\\ 0.997\end{pmatrix}$. (b) $L = 0.2$: $\begin{pmatrix}\mathcal{J}_{\mathrm{MC}}\\ \mathcal{J}_{\mathrm{MPC}}\end{pmatrix} = \begin{pmatrix}0.974\\ 0.998\end{pmatrix}$. (c) $L = 0.3$: $\begin{pmatrix}\mathcal{J}_{\mathrm{MC}}\\ \mathcal{J}_{\mathrm{MPC}}\end{pmatrix} = \begin{pmatrix}0.985\\ 0.983\end{pmatrix}$.

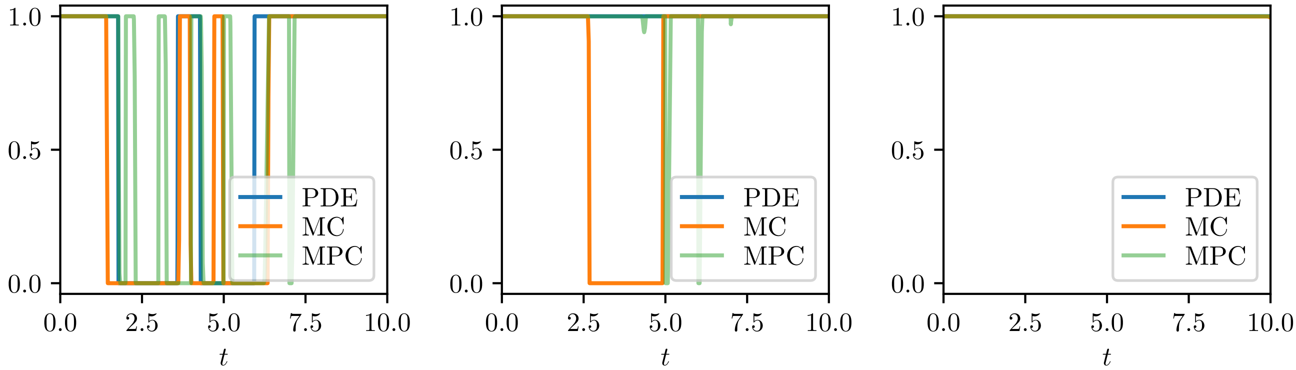

(d) $L = 0.4$: $\begin{pmatrix}\mathcal{J}_{\mathrm{MC}}\\ \mathcal{J}_{\mathrm{MPC}}\end{pmatrix} = \begin{pmatrix}0.989\\ 0.996\end{pmatrix}$. (e) $L = 0.5$: $\begin{pmatrix}\mathcal{J}_{\mathrm{MC}}\\ \mathcal{J}_{\mathrm{MPC}}\end{pmatrix} = \begin{pmatrix}0.992\\ 1.000\end{pmatrix}$. (f) $L = 0.6$: $\begin{pmatrix}\mathcal{J}_{\mathrm{MC}}\\ \mathcal{J}_{\mathrm{MPC}}\end{pmatrix} = \begin{pmatrix}1.000\\ 1.000\end{pmatrix}$.

Figure 9: Optimal controls of the moment problem (65) with $N = 25$ moments, Bernstein approximants of degree $N(a) = N(h) = 4$, default parameters listed in (69), and various Hill parameters L. The optimal controls presented are the open-loop (MC) and closed-loop (MPC) controls for the PDE system (62), whose optimal control (PDE) is detailed in Ref. [31]. For $L \leq 0.2$ the PDE optimal control problems use an additional penalty term $\epsilon \int_0^T (\mathrm{d}u/\mathrm{d}t)^2 \, \mathrm{d}t$ in the cost function with $\epsilon = 10^{-4}$ to regularise high-frequency oscillations.

the zero moment closure. It is worth keeping in mind that the full distribution is found using a numerical method that itself contains some numerical error. Nevertheless, the approximation captures much of the qualitative behaviour of the moments and is very similar to the central Taylor approximation (see fig. 10 in Appendix C). This raises the question, how does this discrepancy manifest in the associated optimal control?

To solve the optimal control problem numerically, we implement a multiple-shooting direct numerical approach based on an Euler discretisation and encoded in CasADi [4], a framework that performs automatic differentiation to produce a nonlinear program equipped with gradient information and solved by the IPOPT solver [54].

It is not straightforward to adapt the zero-information closure to provide gradient information for use in optimal control. Moreover, the zero-information closure seems too slow to be relevant for use in optimal control. Perhaps surprisingly, we were not able to obtain good forward simulation results using the zero-information closure. For all of these reasons, to solve the optimal control problem (65) we are left with the zero and central closures, as well as Bernstein polynomial approximants and Chebyshev interpolants. Remarkably, despite the poor performance of the zero closure for the examples in sections 5 and 6, and despite the Bernstein approximants being suboptimal approximants (in the L^∞ sense) this combination was the only one to exhibit robust convergence. We note that using the Chebyshev interpolants resulted in diverging iterations for all parameter values and closure methods we tried. On the other hand, using Bernstein approximants, the central closure did sometimes converge to a local optimum. In these cases, the result closely matched the local optimum reached using the zero closure. Nevertheless, the central moment closure was significantly more fragile, and small changes in the numbers of moments, the number of time steps, and the initial control guess could result in diverging iterations. Therefore, we illustrate results using Bernstein approximants and the zero moment closure.

To quantify the performance of the optimal control, we introduce the relative performance measure

$$\mathcal{J}_{\mathrm{MC}} := \frac{J_{\mathrm{PDE}}(u_{\mathrm{MC}})}{J_{\mathrm{PDE}}(u_{\mathrm{PDE}})}, \tag{71}$$

denoting the ratio of the objective functions J_{PDE} of the PDE model (62) when applying different controls; u_{MC} denoting the optimal control of the moment-closure system (65) and u_{PDE} denoting the optimal control of the PDE system (62). When the PDE model is considered the ground truth, the performance measure (71) indicates how well the moment-closure model acts as a surrogate model, with the limit of $\mathcal{J}_{\mathrm{MC}} = 1$ being a lossless replacement.

Before diving into the optimal control results, we introduce the closed-loop control u_{MPC} and its associated performance measure $\mathcal{J}_{\mathrm{MPC}}$ defined in analogy with (71). The open-loop control is susceptible to modeling and measurement error, and not robust to real-time changes in the system. Solving the closed-loop problem is challenging as it requires us to solve the Hamilton-Jacobi-Bellman PDE [26]. One popular method to close the loop while avoiding this problem, and thereby remedy these problems to some extent, is to resolve the open-loop problem upon receiving updated state information. This control algorithm is called the receding-horizon control, or model-predictive control (MPC), which is the term we adopt here. In the simulations here, we update the state information in the MPC control at each time unit (modeling an hourly update in the bioreactor system).

In fig. 9 we compare the PDE optimal controls with both the open-loop and closed-loop optimal controls for the moment system. We see that the open-loop controls qualitatively reproduce much of the PDE control structure. There are singular arcs figs. 9a and 9b, and for larger L in figs. 9c and 9d, the moment-closure control reproduces the isolated pulses of the PDE control. This result is a qualitative improvement over the low-order moment-closure approximations studied in Ref. [31] where these features were not faithfully reproduced.

The open-loop performance incurs error of less than 5%. The closed-loop controls find corrections that guarantee performance to within less than 2% error. Again comparing to the errors of the low-order moment-closure approximations in Ref. [31], which are up to 25%, these results demonstrate significant improvement. This observation — that the heterogeneity-preserving higher-order moment system restores near-optimal performance where the homogeneous moment-closure approximation fell short — drives home the importance of heterogeneity, as it demonstrates that the poor homogeneous performance was not the result of using moment equations, but of neglecting the heterogeneity.

Before concluding, we propose a possible explanation for the surprising success of the zero closure. Since the continuum variables (over which we integrate to obtain the moments) are scaled with the characteristic system size, one can ensure that the bulk of the distribution is contained in the hypercube $[0,1]^d$. In this case, it is possible to expect the magnitude of the moments to decrease with increasing order, at least up to some order. It is instructive to have a concrete example in mind. Take a univariate normal distribution centred at zero with variance σ^2. The distribution is symmetric, so odd-ordered moments vanish, however, moments of even order $2i$ are given by $\sigma^{2i}(2i-1)!!$. A plot of this quantity as a function of i shows that the moment value typically decreases until some critical $i = i_0$ after which it increases, eventually diverging (it is straightforward to prove analytically that the moments diverge for all σ as $i \to \infty$).

It seems plausible, then, that a zero truncation of the moment hierarchy, around the critical order $2i_0$, approximately preserves the feature that the moments of orders close to $2i_0$, and their influence on the lower orders, remain small. Therefore, even though the zero closure does not describe a family of continuous distributions (as mentioned earlier, a non-negative continuous distribution of non-zero mass must have strictly positive moments at all order), it is reasonable that it can provide a useful approximation when the moments being closed, and their influence on lower-order moments in the moment hierarchy, are negligible. While this intuition can be immediately extended to the central closure, it is unclear how the nonlinearities introduced (see (37)) by this closure affect the equations analytically or numerically. The weaker results for the central closure might hint at an increased sensitivity that degrades the robustness of the optimisation.

8 Conclusions

Beginning with a modular class of PDE models describing the evolution of cellular populations, we derive and study an associated moment hierarchy approximation. By employing a family of benchmark processes where the moment hierarchies involve no approximation (and for which we have analytical solutions to which to compare), we explain analytically why the zero and central moment-closure approximations fail. We demonstrate how maximum entropy distributions provide a successful moment-closure technique for these systems.

Given this failure of the zero and central closures, that has been demonstrated previously in the discrete master-equation setting, it might be tempting to abandon their use. However, other methods tend to be prohibitively costly when it comes to optimisation. We provide a practically relevant model of a microbial consortium where only the simplest closure (the zero moment closure) provides robust convergence to an accurate solution. Furthermore, this example includes rate functions of non-polynomial form. These forms do not produce a closed hierarchy of moment equations, and previous studies have ignored this additional complexity by not treating such cases. We discuss several systematic polynomial approximation methods that allow us to recover the moment hierarchy. Bernstein polynomials, while not the closest approximants, faithfully preserve features of the original non-polynomial function affording robust convergence in the optimisation routine. On the other hand, the closest approximation typically introduces undesirable oscillations and results in moment equations for which the same optimisation routine diverges wildly.

The purpose of studying high-order moment-closure approximations rather than the full PDE model is to, on the one hand, retain the heterogeneous dynamics that are required to ensure optimal process control, while, on the other hand, enabling a dimension reduction. For this reason it is particularly useful to identify systems where the simple moment closure produces good results. In contrast to more sophisticated closure approaches, it is straightforward to implement and computationally cheap. Although it may require a particularly high-order system (we used 25 moments for this example), the optimal control is still calculated in a number of seconds on a standard laptop computer, while the optimal control of the PDE model is at least an order of magnitude slower.

Another benefit to the moment-closure approach is that, since the state space has been incorporated analytically into the framework, no discretisation is required in the state space, which can introduce non-negligible error into the numerical results. For the optimal controls studied here, the use of the polynomial approximation is a source of error absent in the PDE formulation. However, the PDE formulation studied in Ref. [31] uses finite-differences in the state space, which introduce a new source of error via numerical diffusion.

Appendix

A Moment hierarchy approximation

In this appendix, we detail how the components introduced in section 2 contribute to the moment equations.

A.1 Copy-number population growth

In the copy-number paradigm, we multiply (3) by $\boldsymbol{x}^{\boldsymbol{i}}$ and integrate over the state space to obtain

$$\frac{\mathrm{d}}{\mathrm{d}t}X_k^{\boldsymbol{i}}(t) = -\sum_{|\boldsymbol{j}|\le N(g_k)} g_{k,\boldsymbol{j}}(t)X_k^{\boldsymbol{i}+\boldsymbol{j}}(t) + 2\int_{\mathbb{R}_+^d}\boldsymbol{x}^{\boldsymbol{i}}\int_{\hat{\boldsymbol{x}}\ge\boldsymbol{x}} g_k(\hat{\boldsymbol{x}},t)p_k(\hat{\boldsymbol{x}},t)\theta_k(\boldsymbol{x}\mid\hat{\boldsymbol{x}})\,\mathrm{d}\hat{\boldsymbol{x}}\,\mathrm{d}\boldsymbol{x} + (\text{Non-growth sources}), \tag{72}$$

where, changing the order of integration, and leveraging self-similarity (5), we see that

$$\begin{aligned}\int_{\mathbb{R}_+^d}\boldsymbol{x}^{\boldsymbol{i}}\int_{\hat{\boldsymbol{x}}\ge\boldsymbol{x}} g_k(\hat{\boldsymbol{x}},t)p_k(\hat{\boldsymbol{x}},t)\theta_k(\boldsymbol{x}\mid\hat{\boldsymbol{x}})\,\mathrm{d}\hat{\boldsymbol{x}}\,\mathrm{d}\boldsymbol{x} &= \int_{\mathbb{R}_+^d} g_k(\hat{\boldsymbol{x}},t)p_k(\hat{\boldsymbol{x}},t)\int_{\boldsymbol{0}\le\boldsymbol{x}\le\hat{\boldsymbol{x}}}\boldsymbol{x}^{\boldsymbol{i}}\theta_k(\boldsymbol{x}\mid\hat{\boldsymbol{x}})\,\mathrm{d}\boldsymbol{x}\,\mathrm{d}\hat{\boldsymbol{x}}\\ &= \int_{\mathbb{R}_+^d}\hat{\boldsymbol{x}}^{\boldsymbol{i}} g_k(\hat{\boldsymbol{x}},t)p_k(\hat{\boldsymbol{x}},t)\int_{\boldsymbol{0}\le\boldsymbol{y}\le\boldsymbol{1}}\boldsymbol{y}^{\boldsymbol{i}}\Theta_k(\boldsymbol{y})\,\mathrm{d}\boldsymbol{y}\,\mathrm{d}\hat{\boldsymbol{x}}\\ &= \Theta_k^{\boldsymbol{i}}\sum_{|\boldsymbol{j}|\le N(g_k)} g_{k,\boldsymbol{j}}(t)X_k^{\boldsymbol{i}+\boldsymbol{j}}(t).\end{aligned} \tag{73}$$

for

$$\Theta_k^{\boldsymbol{i}} := \int_{\boldsymbol{0}\le\boldsymbol{y}\le\boldsymbol{1}}\boldsymbol{y}^{\boldsymbol{i}}\Theta_k(\boldsymbol{y})\,\mathrm{d}\boldsymbol{y}. \tag{74}$$

The contributions in (20) follow.

Some moments $\Theta_k^{\boldsymbol{i}}$ may be calculated in terms of lower-order moments using symmetry:

$$\begin{aligned}\Theta_k^{\boldsymbol{i}} = \int_{\boldsymbol{0}\le\boldsymbol{y}\le\boldsymbol{1}}\boldsymbol{y}^{\boldsymbol{i}}\Theta_k(\boldsymbol{y})\,\mathrm{d}\boldsymbol{y} = \int_{\boldsymbol{0}\le\boldsymbol{y}\le\boldsymbol{1}}\boldsymbol{y}^{\boldsymbol{i}}\Theta_k(\boldsymbol{1}-\boldsymbol{y})\,\mathrm{d}\boldsymbol{y} &= \int_{\boldsymbol{0}\le\boldsymbol{y}\le\boldsymbol{1}}(\boldsymbol{1}-\boldsymbol{y})^{\boldsymbol{i}}\Theta_k(\boldsymbol{y})\,\mathrm{d}\boldsymbol{y}\\ &= \int_{\boldsymbol{0}\le\boldsymbol{y}\le\boldsymbol{1}}\left(\prod_{j=1}^{d}(1-y_j)^{i_j}\right)\Theta_k(\boldsymbol{y})\,\mathrm{d}\boldsymbol{y}\\ &= \int_{\boldsymbol{0}\le\boldsymbol{y}\le\boldsymbol{1}}\left(\prod_{j=1}^{d}\left[\sum_{k=0}^{i_j}\binom{i_j}{k}(-1)^k y_j^k\right]\right)\Theta_k(\boldsymbol{y})\,\mathrm{d}\boldsymbol{y}\\ &= (-1)^{|\boldsymbol{i}|}\Theta_k^{\boldsymbol{i}} + \sum_{\boldsymbol{j}<\boldsymbol{i}} c_{\boldsymbol{j}}\Theta_k^{\boldsymbol{j}},\end{aligned} \tag{75}$$

where $\boldsymbol{j} < \boldsymbol{i}$ denotes the set of multi-indices $\{\boldsymbol{j} \mid \forall m : j_m \leq i_m,\ \exists m : j_m < i_m\}$ and $c_{\boldsymbol{j}}$ are integer coefficients. Therefore, for odd orders $|\boldsymbol{i}|$, we have

$$\Theta_k^{\boldsymbol{i}} = \frac{1}{2} \sum_{\boldsymbol{j}<\boldsymbol{i}} c_{\boldsymbol{j}} \Theta_k^{\boldsymbol{j}}. \tag{76}$$

A.2 Continuum dynamics

The contributions stemming from the Fokker–Planck terms (13) can be derived by expressing the operator in divergence form, namely,

$$\frac{\partial}{\partial t} p_k(\boldsymbol{x}, t) = -\nabla \cdot \boldsymbol{\Phi}_k(\boldsymbol{x}, t) + (\text{other sources}), \tag{77}$$

for the flux $\boldsymbol{\Phi}_k(\boldsymbol{x}, t)$ given by

$$\boldsymbol{\Phi}_k(\boldsymbol{x}, t) = \boldsymbol{e}_k \left\{ r_k(\boldsymbol{x}, t) p_k(\boldsymbol{x}, t) - \frac{1}{2\Omega} \boldsymbol{e}_k \cdot \nabla \left[r_k(\boldsymbol{x}, t) p_k(\boldsymbol{x}, t) \right] \right\}. \tag{78}$$

By application of the divergence theorem, and using the zero normal flux boundary condition (14), it follows that there are no zeroth-order contributions ($\boldsymbol{i} = \boldsymbol{0}$). This reflects the fact that the process describes a change in the continuum species, but not the population mass. By application of Green's identities, we find, for $|\boldsymbol{i}| > 0$, that

$$\begin{aligned}
&- \int_{\mathbb{R}_+^d} \boldsymbol{x}^{\boldsymbol{i}} \nabla \cdot \boldsymbol{\Phi}_k(\boldsymbol{x}, t) \, \mathrm{d}\boldsymbol{x} \\
&\quad = \int_{\mathbb{R}_+^d} \left(\nabla \boldsymbol{x}^{\boldsymbol{i}} \cdot \boldsymbol{e}_k \right) \left\{ r_k(\boldsymbol{x}, t) p_k(\boldsymbol{x}, t) - \frac{1}{2\Omega} \boldsymbol{e}_k \cdot \nabla \left[r_k(\boldsymbol{x}, t) p_k(\boldsymbol{x}, t) \right] \right\} \mathrm{d}\boldsymbol{x} \\
&\quad \approx \int_{\mathbb{R}_+^d} \left(\sum_{\ell=1}^{d} i_\ell e_{k,\ell} \boldsymbol{x}^{\boldsymbol{i}-\boldsymbol{v}_\ell} \right) r_k(\boldsymbol{x}, t) p_k(\boldsymbol{x}, t) + \frac{1}{2\Omega} \left(r_k(\boldsymbol{x}, t) p_k(\boldsymbol{x}, t) \boldsymbol{e}_k \cdot \nabla \left(\nabla \boldsymbol{x}^{\boldsymbol{i}} \cdot \boldsymbol{e}_k \right) \right) \mathrm{d}\boldsymbol{x} \\
&\quad = \sum_{\ell=1}^{d} i_\ell e_{k,\ell} \int_{\mathbb{R}_+^d} \boldsymbol{x}^{\boldsymbol{i}-\boldsymbol{v}_\ell} r_k(\boldsymbol{x}, t) p_k(\boldsymbol{x}, t) \, \mathrm{d}\boldsymbol{x} + \frac{1}{2\Omega} \sum_{\ell=1}^{d} \sum_{m=1}^{d} i_\ell (i_m - \delta_{\ell m}) e_{k,\ell} e_{k,m} \int_{\mathbb{R}_+^d} \boldsymbol{x}^{\boldsymbol{i}-\boldsymbol{v}_\ell-\boldsymbol{v}_m} r_k(\boldsymbol{x}, t) p_k(\boldsymbol{x}, t) \, \mathrm{d}\boldsymbol{x} \\
&\quad \approx \sum_{\ell=1}^{d} i_\ell e_{k,\ell} \sum_{|\boldsymbol{j}| \leq N(r_k)} r_{k,\boldsymbol{j}}(t) X_k^{\boldsymbol{i}-\boldsymbol{v}_\ell+\boldsymbol{j}}(t) + \frac{1}{2\Omega} \sum_{\ell=1}^{d} \sum_{m=1}^{d} i_\ell (i_m - \delta_{\ell m}) e_{k,\ell} e_{k,m} \sum_{|\boldsymbol{j}| \leq N(r_k)} r_{k,\boldsymbol{j}}(t) X_k^{\boldsymbol{i}-\boldsymbol{v}_\ell-\boldsymbol{v}_m+\boldsymbol{j}}(t),
\end{aligned} \tag{79}$$

where $\delta_{\ell m}$ is the Kronecker Delta function, that takes the value one when $\ell = m$ and zero otherwise, $e_{k,\ell}$ denotes the ℓth component of the vector $\boldsymbol{e}_k$, and $\boldsymbol{v}_\ell$ denotes the vector of zeros except for the ℓth component whose value is one. The first approximation stems from ignoring boundary contributions (these are small if the density is small at the boundaries since the term has a coefficient of $\mathcal{O}(1/\Omega)$), while the second approximation stems from the polynomial approximation. The form in (25) follows.

The bursty production (15) similarly has no zeroth-order contribution. To see this, note that the zeroth-order terms sum all possible jumps — for each $\boldsymbol{x}$ add all the valid jumps *to* $\boldsymbol{x}$ — which may be expressed from the dual perspective — for each $\boldsymbol{x}$ add all the valid jumps *from* $\boldsymbol{x}$. Then, utilising (16), we find that

$$\begin{aligned}
\|\boldsymbol{e}_k\| &\int_{\mathbb{R}_+^d} \int_{\boldsymbol{x}-z\boldsymbol{e}_k \in \mathbb{R}_+^d} f_k(\boldsymbol{x} - z\boldsymbol{e}_k, t) p_k(\boldsymbol{x} - z\boldsymbol{e}_k, t) Q_k(\boldsymbol{x} - z\boldsymbol{e}_k, z\|\boldsymbol{e}_k\|) \, \mathrm{d}z \, \mathrm{d}\boldsymbol{x} \\
&= \int_{\mathbb{R}_+^d} f_k(\boldsymbol{x}, t) p_k(\boldsymbol{x}, t) \int_0^\infty \|\boldsymbol{e}_k\| Q_k(\boldsymbol{x}, z\|\boldsymbol{e}_k\|) \, \mathrm{d}z \, \mathrm{d}\boldsymbol{x} \\
&= \int_{\mathbb{R}_+^d} f_k(\boldsymbol{x}, t) p_k(\boldsymbol{x}, t) \, \mathrm{d}\boldsymbol{x}.
\end{aligned} \tag{80}$$

For the calculation of general order $\boldsymbol{i}$, we perform a preliminary binomial expansion for vectors $\boldsymbol{x}$ and $\boldsymbol{y}$ and the multi-index $\boldsymbol{i}$:

$$(\boldsymbol{x} + \boldsymbol{y})^{\boldsymbol{i}} = \prod_{j=1}^{d} (x_j + y_j)^{i_j} = \prod_{j=1}^{d} \left(\sum_{\ell=0}^{i_j} \binom{i_j}{\ell} x_j^\ell y_j^{i_j-\ell} \right) = \sum_{\boldsymbol{j} \leq \boldsymbol{i}} b_{\boldsymbol{i},\boldsymbol{j}} \boldsymbol{x}^{\boldsymbol{j}} \boldsymbol{y}^{\boldsymbol{i}-\boldsymbol{j}}, \tag{81}$$

for some integer coefficients $b_{\boldsymbol{i},\boldsymbol{j}}$, where $b_{\boldsymbol{i},\boldsymbol{i}} = 1$. Then, again appealing to the dual perspective, we evaluate the integral:

$$\begin{aligned}
&\int_{\mathbb{R}^d_+} \boldsymbol{x}^{\boldsymbol{i}} \|\boldsymbol{e}_k\| \int_{\boldsymbol{x}-z\boldsymbol{e}_k \in \mathbb{R}^d_+} f_k(\boldsymbol{x} - z\boldsymbol{e}_k, t) p_k(\boldsymbol{x} - z\boldsymbol{e}_k, t) Q(\boldsymbol{x} - z\boldsymbol{e}_k, z\|\boldsymbol{e}_k\|) \,\mathrm{d}z \,\mathrm{d}\boldsymbol{x} \\
&\qquad = \int_{\mathbb{R}^d_+} \int_{\boldsymbol{x}-z\boldsymbol{e}_k \in \mathbb{R}^d_+} (\boldsymbol{x} - z\boldsymbol{e}_k + z\boldsymbol{e}_k)^{\boldsymbol{i}} \|\boldsymbol{e}_k\| f_k(\boldsymbol{x} - z\boldsymbol{e}_k, t) p_k(\boldsymbol{x} - z\boldsymbol{e}_k, t) Q_k(\boldsymbol{x} - z\boldsymbol{e}_k, z\|\boldsymbol{e}_k\|) \,\mathrm{d}z \,\mathrm{d}\boldsymbol{x} \\
&\qquad = \sum_{\boldsymbol{j} \leq \boldsymbol{i}} b_{\boldsymbol{i},\boldsymbol{j}} \boldsymbol{e}_k^{\boldsymbol{i}-\boldsymbol{j}} \int_{\mathbb{R}^d_+} \int_{\boldsymbol{x}-z\boldsymbol{e}_k \in \mathbb{R}^d_+} (\boldsymbol{x} - z\boldsymbol{e}_k)^{\boldsymbol{j}} z^{|\boldsymbol{i}-\boldsymbol{j}|} \|\boldsymbol{e}_k\| f_k(\boldsymbol{x} - z\boldsymbol{e}_k, t) p_k(\boldsymbol{x} - z\boldsymbol{e}_k, t) Q_k(\boldsymbol{x} - z\boldsymbol{e}_k, z\|\boldsymbol{e}_k\|) \,\mathrm{d}z \,\mathrm{d}\boldsymbol{x} \\
&\qquad = \sum_{\boldsymbol{j} \leq \boldsymbol{i}} b_{\boldsymbol{i},\boldsymbol{j}} \boldsymbol{e}_k^{\boldsymbol{i}-\boldsymbol{j}} \int_{\mathbb{R}^d_+} \boldsymbol{x}^{\boldsymbol{j}} f_k(\boldsymbol{x}, t) p_k(\boldsymbol{x}, t) \int_0^\infty z^{|\boldsymbol{i}-\boldsymbol{j}|} \|\boldsymbol{e}_k\| Q_k(\boldsymbol{x}, z\|\boldsymbol{e}_k\|) \,\mathrm{d}z \,\mathrm{d}\boldsymbol{x} \\
&\qquad = \sum_{\boldsymbol{j} \leq \boldsymbol{i}} b_{\boldsymbol{i},\boldsymbol{j}} \boldsymbol{e}_k^{\boldsymbol{i}-\boldsymbol{j}} \|\boldsymbol{e}_k\|^{-|\boldsymbol{i}-\boldsymbol{j}|} \int_{\mathbb{R}^d_+} \boldsymbol{x}^{\boldsymbol{j}} Q_{k,|\boldsymbol{i}-\boldsymbol{j}|}(\boldsymbol{x}) f_k(\boldsymbol{x}, t) p_k(\boldsymbol{x}, t) \,\mathrm{d}\boldsymbol{x},
\end{aligned} \tag{82}$$

where we have defined, for $j \in \mathbb{N}_0$,

$$Q_{k,j}(\boldsymbol{x}) := \int_0^\infty y^j Q_k(\boldsymbol{x}, y) \,\mathrm{d}y. \tag{83}$$

Recalling that $b_{\boldsymbol{i},\boldsymbol{i}} = 1$, we deduce the general form in (26).

B Moments from a discrete and continuum formulation

In this appendix, we compare the moment hierarchies obtained from a discrete and continuum formulation of a single-cell birth process:

$$\varnothing \quad \xrightarrow{\lambda} \quad \mathrm{X}, \tag{84}$$

where the birth rate λ is constant.

We start with the continuum formulation, which takes the Fokker–Planck form

$$\frac{\partial}{\partial t} p(x, t) = -\frac{\partial}{\partial x}[\lambda p(x, t)] + \frac{1}{2\Omega} \frac{\partial^2}{\partial x^2}[\lambda p(x, t)], \tag{85}$$

subject to the boundary conditions

$$\lambda p(x, t) - \frac{1}{2\Omega} \frac{\partial}{\partial x}[\lambda p(x, t)] = 0 \qquad\qquad \text{at } x = 0 \text{ and as } x \to \infty. \tag{86}$$

For the ith moment

$$X^i(t) := \int_0^\infty x^i p(x, t) \,\mathrm{d}x, \tag{87}$$

the dynamics are obtained by multiplying equation (85) by x^i and integrating over the domain $\mathbb{R}_+$, whereby, after integrating by parts and substituting the boundary conditions (86), we find that

$$\begin{aligned}
\dot{X}^i(t) &= i\lambda X^{i-1}(t) + \frac{i(i-1)}{2\Omega} \lambda X^{i-2}(t) - \frac{1}{2\Omega} \left[i x^{i-1} \frac{\partial}{\partial x}[\lambda p(x, t)] \right]_0^\infty \\
&\approx i\lambda X^{i-1}(t) + \frac{i(i-1)}{2\Omega} \lambda X^{i-2}(t).
\end{aligned} \tag{88}$$

We neglect the $\mathcal{O}(1/\Omega)$ boundary term, which we expect to be negligible if the probability distribution is concentrated away from the domain boundaries. On the other hand, we retain the $\mathcal{O}(1/\Omega)$ contribution of the second term on the right-hand side of (88), which stems from a singular perturbation of the PDE, and thus is expected to impact the distribution (as we demonstrate in section 5).

The discrete formulation involves the chemical master equation governing the law $p_n(t)$, representing the probability of the cell being in discrete state n at time t, which given by [28]

$$\dot{p}_n(t) = -\hat{\lambda} p_n(t) + \hat{\lambda} p_{n-1}(t). \tag{89}$$

We have adopted a scaled reaction rate $\hat{\lambda} \propto \lambda$ for reasons that will become clear. Further, we adopt the convention that $p_n(t)$ is identically zero for all $n < 0$. The dynamics of the discrete moments

$$Y^i(t) := \sum_{n \geq 0} n^i p_n(t), \tag{90}$$

are obtained by multiplying equation (89) by n^i and summing, which yields

$$\begin{aligned}
\dot{Y}^i(t) &= -\hat{\lambda} \sum_{n \geq 0} n^i p_n(t) + \hat{\lambda} \sum_{n \geq 0} n^i p_{n-1}(t) \\
&= -\hat{\lambda} Y^i(t) + \hat{\lambda} \sum_{n \geq 0} \sum_{j=0}^{i} \binom{i}{j} (n-1)^j p_{n-1}(t) \\
&= -\hat{\lambda} Y^i(t) + \hat{\lambda} \sum_{j=0}^{i} \binom{i}{j} Y^j(t) \\
&= \hat{\lambda} \sum_{j=0}^{i-1} \binom{i}{j} Y^j(t).
\end{aligned} \tag{91}$$

At first sight, the discrete moment hierarchy (91) does not appear to resemble the continuum hierarchy (88). However, an appropriate scaling reveals how the continuum hierarchy approximates the discrete hierarchy. To see this, consider a characteristically large discrete system size $\Omega \gg 1$. In this case, it is reasonable to expect the ith moment to be of order $\mathcal{O}(\Omega^i)$, since the probability mass is expected to be distributed predominantly in states n of order $\mathcal{O}(\Omega)$. This motivates the scaled discrete moment and scaled discrete state variable, given respectively by

$$Z^i(t) := \frac{Y^i(t)}{\Omega^i}, \qquad\qquad z := \frac{n}{\Omega}. \tag{92}$$

Under the state scaling (92), we may deduce the appropriate reaction rate scaling. The rate scaling must preserve the typical time for a characteristic change of state. In the continuum scaling (85), a rate λ drives an $\mathcal{O}(1)$ change of state x on a timescale of $1/\lambda$. In the discrete formulation (89), an $\mathcal{O}(1)$ change of state n occurs on a timescale of $1/\hat{\lambda}$, which, by (92), corresponds to a change of continuum state of order $\mathcal{O}(1/\Omega)$. Therefore, to ensure these two representations are consistent, we require that

$$\hat{\lambda} := \Omega \lambda. \tag{93}$$

Ultimately, we have introduced scalings (92) and (93) that transform the discrete formulation to $\mathcal{O}(1)$ magnitudes. It is instructive to investigate the dynamics of the scaled moments. Substituting (92) into (91), we see that

$$\dot{Z}^i(t) = \lambda \sum_{j=0}^{i-1} \binom{i}{j} \Omega^{j-i+1} Z^j(t) = i\lambda Z^{i-1}(t) + \frac{i(i-1)}{2\Omega} \lambda Z^{i-2}(t) + \mathcal{O}\left(\frac{1}{\Omega^2}\right). \tag{94}$$

Since the moments are of order unity, we have justified why the higher order terms are negligible and quantified the discrepancy. Moreover, the absence of boundary terms in the discrete formulation suggests that the neglected boundary term in (88) is merely an artefact. Crucially, we have shown that the discrete moment hierarchy (91) approximately satisfies the continuum moment hierarchy dynamics (88). We deduce that studying the moments of the Fokker–Planck approximation, rather than the moments of the discrete formulation in this one-dimensional setting results in a negligible $\mathcal{O}(1/\Omega^2)$ discrepancy. It is common that $\Omega \gg 1$ (in the case studies in this work $\Omega \geq 1000$), which produces errors typically no larger than the other numerical operations (such as those resulting from discretising the ODEs or convergence tolerance in optimisation routines).

For the continuum bursts introduced in section 2.4 the situation is more straightforward since the contributions to the moment hierarchy are exact, and of identical form, in both the discrete and continuum formulations. The discrepancy is thus only in the burst parameters, which can be shown to coincide in both formulations up to $\mathcal{O}(1/\Omega)$. Therefore, we expect any discrepancy to become important only when the certainty on our parameters is smaller than this magnitude, which is typically not realised in real-world scenarios.

In summary, we do not expect important differences between these two system formulations, and thus prefer to leverage the advantage of studying the moments of the continuum formulation for which extended simulation tools are available for their simulation with real-world system sizes.

C Taylor-expansion central moment equations

In this appendix, we formulate a system of central moment equations of the consortium model (62) based on a truncated Taylor expansion of the nonlinear propensities. The idea is analogous to the non-central moment equations discussed in section 3, except the moments and polynomial approximations are centred about the distribution means.

We begin by defining the shifted moments

$$\hat{X}^i(t) := \int_0^\infty (x - m_x(t))^i g(x,t)\,\mathrm{d}x, \qquad \hat{Y}^i(t) := \int_0^\infty (y - m_y(t))^i p(y,t)\,\mathrm{d}y, \tag{95}$$

for arbitrary functions $m_x(t)$ and $m_y(t)$.

Next, we Taylor expand the nonlinear propensities in equations (62a) and (62b) about $m_x(t)$ and $m_y(t)$, respectively:

$$\begin{aligned} h(x) &\approx \sum_{j=0}^{N(h)} \frac{h^{(j)}(m_x(t))}{j!}(x - m_x(t))^j =: \sum_{j=0}^{N(h)} \hat{h}_j(m_x(t))(x - m_x(t))^j, \\ a(y) &\approx \sum_{j=0}^{N(a)} \frac{a^{(j)}(m_y(t))}{j!}(y - m_y(t))^j =: \sum_{j=0}^{N(a)} \hat{a}_j(m_y(t))(y - m_y(t))^j. \end{aligned} \tag{96}$$

Multiplying equations (62a) and (62b) by $(x - m_x(t))^i$ and $(y - m_y(t))^i$, respectively, and applying the same approximation techniques as developed for the non-shifted moment systems, we find that the shifted moments satisfy

$$\begin{aligned} \frac{\mathrm{d}}{\mathrm{d}t}\hat{X}^i(t) = {}& -i\hat{X}^{i-1}(t)\dot{m}_x(t) + A\hat{X}^i(t) - \Lambda(t)\hat{X}^i(t) - fu(t)\sum_{j=0}^{N(h)} \hat{h}_j(m_x(t))\hat{X}^{j+i}(t) \\ & + i\left[\alpha\hat{X}^{i-1}(t) - \beta\left(\hat{X}^i(t) + m_x(t)\hat{X}^{i-1}(t)\right)\right] + \frac{i(i-1)}{2\Omega}\left[\alpha\hat{X}^{i-2}(t) + \beta\left(\hat{X}^{i-1}(t) + m_x(t)\hat{X}^{i-2}(t)\right)\right], \end{aligned} \tag{97a}$$

$$\begin{aligned} \frac{\mathrm{d}}{\mathrm{d}t}\hat{Y}^i(t) = {}& -i\hat{Y}^{i-1}(t)\dot{m}_y(t) + \sum_{j=0}^{N(a)} \hat{a}_j(m_y(t))\hat{Y}^{j+i}(t) - \Lambda(t)\hat{Y}^i(t) + (-m_y(t))^i fu(t)\sum_{j=0}^{N(h)} \hat{h}_j(m_x(t))\hat{X}^j(t) \\ & + i\left[\mu\hat{Y}^{i-1}(t) - \nu\left(\hat{Y}^i(t) + m_y(t)\hat{Y}^{i-1}(t)\right)\right] + \frac{i(i-1)}{2\Omega}\left[\mu\hat{Y}^{i-2}(t) + \nu\left(\hat{Y}^{i-1}(t) + m_y(t)\hat{Y}^{i-2}(t)\right)\right], \end{aligned} \tag{97b}$$

$$\Lambda(t) = A\hat{X}^0(t) + \sum_{j=0}^{N(a)} \hat{a}_j(m_y(t))\hat{Y}^j(t). \tag{97c}$$

The form of equations (97a) and (97b) is similar of the non-shifted moment formulation (65) with some perturbations due to the moments being shifted to a non-zero, time-varying point.

The initial conditions of system (97a) and (97b) are given by the steady state solution in the absence of light ($u(t) = 0$) with no producers. To determine these initial conditions, we need to specify the functions $m_x(t)$ and $m_y(t)$, which we take as the means of each distribution $g(x,t)$ over x and $p(y,t)$ over y, namely

$$m_x(t) = \frac{X^1(t)}{\hat{X}^0(t)}, \qquad m_y(t) = \frac{Y^1(t)}{\hat{Y}^0(t)}, \tag{97d}$$

where $X^1(t)$ and $Y^1(0)$ are the non-shifted moments defined in (63). We thus refer to the moments as *central moments*. Note that the central and non-central zeroth-order moments coincide by definition: $X^0(t) = \hat{X}^0(t)$ and $Y^0(t) = \hat{Y}^0(t)$. Moreover, the first-order central moment vanishes identically by definition, since

$$\hat{X}^1(t) = \int_0^\infty \left(x - \frac{X^1(t)}{\hat{X}^0(t)}\right) g(x,t)\,\mathrm{d}x = X^1(t) - \frac{X^1(t)}{\hat{X}^0(t)}\hat{X}^0(t) = 0, \tag{97e}$$

and similarly $\hat{Y}^1(t) = 0$.

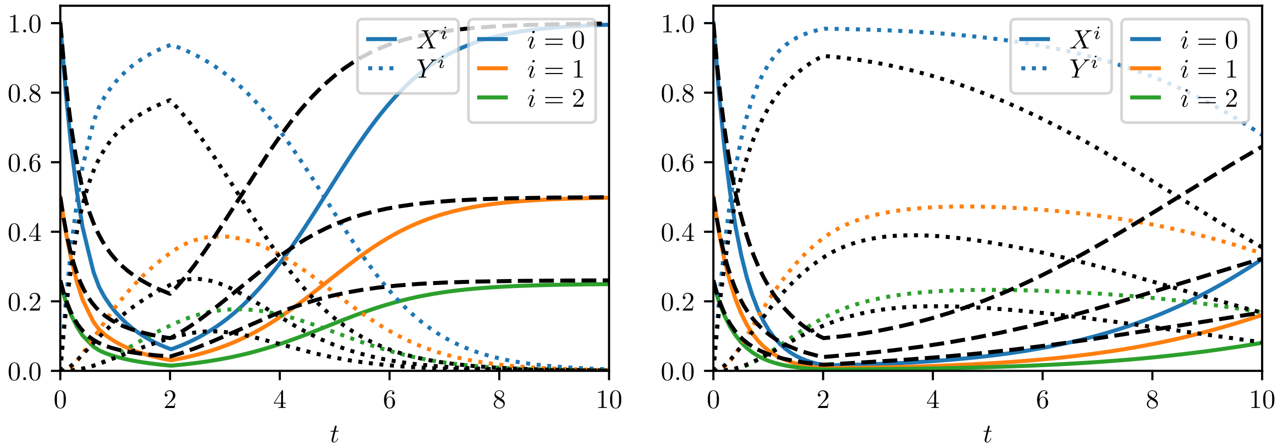

(a) $L = 0.1$.

(b) $L = 0.5$.

Figure 10: Moments of the full distribution (black curves) governed by (62) (solved using the discretisation from Ref. [31]) compared to solution of the central moment equations (coloured curves) governed by (97) and using a central moment closure via truncating at $N = 10$ moments. The black dashed curves correspond to moments $X^i(t)$ while the black dotted curves correspond to $Y^i(t)$. The light profile (70) was employed, for various Hill parameters L and the default parameters in (69).

This formulation requires that we track the non-central first-order moments. The governing equations may be written in a manner consistent with the central moment formulation, namely

$$\frac{\mathrm{d}}{\mathrm{d}t}X^1(t) = AX^1(t) - \Lambda(t)X^1(t) - fu(t)\sum_{j=0}^{N(h)} \hat{h}_j(m_x(t))\left(\hat{X}^{j+i}(t) + \frac{X^1(t)}{\hat{X}^0(t)}\hat{X}^j(t)\right) + \alpha\hat{X}^0(t) - \beta X^1(t), \tag{97f}$$

$$\frac{\mathrm{d}}{\mathrm{d}t}Y^1(t) = \sum_{j=0}^{N(a)} \hat{a}_j(m_y(t))\left(\hat{Y}^{j+1}(t) + \frac{Y^1(t)}{\hat{Y}^0(t)}\hat{Y}^j(t)\right) - \Lambda(t)Y^1(t) + \mu Y^0(t) - \nu Y^1(t). \tag{97g}$$

The right-hand sides of (97f) and (97g) depend only on $\{\hat{X}^0(t), \ldots, \hat{X}^N(t), X^1(t), \hat{Y}^0(t), \ldots, \hat{Y}^N(t), Y^1(t)\}$.

We may now determine the initial conditions by seeking the steady state of (97) with no light input and no initial producers, whereby $\hat{Y}^i = Y^1 = 0$ for all i. Setting time derivatives to zero, we find that

$$0 = A\hat{X}^i - \Lambda\hat{X}^i + i\left[\alpha\hat{X}^{i-1} - \beta\left(\hat{X}^i + \frac{X^1}{\hat{X}^0}\hat{X}^{i-1}\right)\right] + \frac{i(i-1)}{2\Omega}\left[\alpha\hat{X}^{i-2} + \beta\left(\hat{X}^{i-1} + \frac{X^1}{\hat{X}^0}\hat{X}^{i-2}\right)\right], \tag{98}$$

where $\Lambda = A\hat{X}^0$. For $i = 0$, we deduce that $0 = A\hat{X}^0(1 - \hat{X}^0)$, and hence $\hat{X}^0 = 1$, since the zero solution is not physically feasible for non-negative growth rates. It follows that $\Lambda = A$ and the growth terms vanish. For $i = 1$, we find that

$$X^1 = \frac{\alpha}{\beta}. \tag{99}$$

For $i \geq 2$, we deduce the recurrence relation

$$\hat{X}^i = \frac{i-1}{2\Omega}\left(\hat{X}^{i-1} + \frac{2\alpha}{\beta}\hat{X}^{i-2}\right), \tag{100}$$

which defines the initial conditions up to arbitrary order N using the initial conditions $\hat{X}^1 = 0$ and $\hat{X}^0 = 1$.

Finally, the objective function (62g) takes the moment form

$$J_{\mathrm{MC}} = Y^1(T) + \int_0^T \Lambda(t)Y^1(t)\,\mathrm{d}t. \tag{101}$$

A “zero” moment closure in this formulation is equivalent to what we refer to as a central moment closure. For the sake of comparison to fig. 8, we plot the non-central moments, which are given by expressing the central moments (95) in terms of the non-central moments (63)

$$\hat{X}^i(t) = \int_0^\infty \left(x - \frac{X^1(t)}{\hat{X}^0(t)}\right)^i g(x,t)\,\mathrm{d}x = X^i(t) + \sum_{j=0}^{i-1}\binom{i}{j}X^j(t)\left(\frac{X^1(t)}{\hat{X}^0(t)}\right)^{i-j}. \tag{102}$$

The identity (102) may be inverted to give $X^i(t)$ in terms of $\hat{X}^i(t)$ (and lower-order moments $\{X^j(t)\}$ for $j < i$).

In fig. 10, we plot the moments of the forward problem solved using the central moment hierarchy and truncated Taylor expansion approximations (97), with the light control profile (70), in analogy with fig. 8. The moments are very similar to those obtained using the Bernstein polynomial approximations with the non-central moment hierarchy and a zero moment closure (fig. 8). The central system with Taylor approximations has a slightly closer agreement with the moments of the full PDE distribution.

The results were robust to the order N of the moment truncation, but less so to the degrees of the Taylor series truncation $N(h)$ and $N(a)$. From $N(h) = N(a) = 4$ there was a noticeable deterioration in performance due to the manifestation of numerical instabilities. This compromises the approximation: low-degree polynomials must be used, however, these only provide good agreement with original non-polynomial function in a narrow vicinity of the mean. We were unable to find convergent results (for any polynomial degree) using this approach for the optimal control problem.

References

[1] C. Aditya, F. Bertaux, G. Batt, and J. Ruess. Using single-cell models to predict the functionality of synthetic circuits at the population scale. *P. Natl. Acad. Sci. USA*, 119(11):e2114438119, 2022.

[2] A. Ale, P. Kirk, and M. P. H. Stumpf. A general moment expansion method for stochastic kinetic models. *J. Chem. Phys.*, 138(17):174101, 2013.

[3] S. J. Altschuler and L. F. Wu. Cellular heterogeneity: do differences make a difference? *Cell*, 141(4):559–563, 2010.

[4] J. A. E. Andersson, J. Gillis, G. Horn, J. B. Rawlings, and M. Diehl. CasADi: a software framework for nonlinear optimization and optimal control. *Math. Program. Comput.*, 11(1):1–36, 2019.

[5] A. Andreychenko, L. Mikeev, and V. Wolf. Model reconstruction for moment-based stochastic chemical kinetics. *ACM T. Model. Comput. S.*, 25(2):1–19, 2015.

[6] K. Brenner, L. You, and F. H. Arnold. Engineering microbial consortia: a new frontier in synthetic biology. *Trends Biotechnol.*, 26(9):483–489, 2008.

[7] A. Brock, H. Chang, and S. Huang. Non-genetic heterogeneity—a mutation-independent driving force for the somatic evolution of tumours. *Nat. Rev. Genet.*, 10(5):336–342, 2009.

[8] G. D. Byrne and A. C. Hindmarsh. A polyalgorithm for the numerical solution of ordinary differential equations. *ACM Trans. Math. Softw.*, 1(1):71—-96, mar 1975.

[9] D. A. Charlebois, K. Hauser, S. Marshall, and G. Balázsi. Multiscale effects of heating and cooling on genes and gene networks. *P. Natl. Acad. Sci. USA*, 115(45):E10797–E10806, 2018.

[10] P. J. Davis. *Interpolation and approximation.* Dover Publications, 1975.

[11] J. B. Deris, M. Kim, Z. Zhang, H. Okano, R. Hermsen, A. Groisman, and T. Hwa. The innate growth bistability and fitness landscapes of antibiotic-resistant bacteria. *Science*, 342(6162):1237435, 2013.

[12] L. Duso and C. Zechner. Stochastic reaction networks in dynamic compartment populations. *Proc. Natl. Acad. Sci. U.S.A.*, 2020.

[13] S. Engblom. Computing the moments of high dimensional solutions of the master equation. *Appl. Math. Comput.*, 180(2):498–515, 2006.

[14] N. Friedman, L. Cai, and X. S. Xie. Linking stochastic dynamics to population distribution: An analytical framework of gene expression. *Phys. Rev. Lett.*, 97:168302, Oct 2006.

[15] E. Hairer, S. P. Norsett, and G. Wanner. Solving ordinary differential equations i: Nonstiff problems. *SIAM Rev.*, 32(3):485, 1990.

[16] J. Harmand, C. Lobry, A. Rapaport, and T. Sari. *The chemostat: Mathematical theory of microorganism cultures.* John Wiley & Sons, USA, 2017.

[17] J. Harmand, C. Lobry, A. Rapaport, and T. Sari. *Optimal Control in Bioprocesses: Pontryagin's Maximum Principle in Practice.* John Wiley & Sons, USA, 2019.

[18] S. Huang. Non-genetic heterogeneity of cells in development: more than just noise. *Development*, 136(23):3853–3862, 2009.

[19] A. Kazeroonian, F. J. Theis, and J. Hasenauer. Modeling of stochastic biological processes with non-polynomial propensities using non-central conditional moment equation. *IFAC P. Vol.*, 47(3):1729–1735, 2014.

[20] S. Klumpp, Z. Zhang, and T. Hwa. Growth rate-dependent global effects on gene expression in bacteria. *Cell*, 139(7):1366–1375, 2009.

[21] J. Kuntz, P. Thomas, G.-B. Stan, and M. Barahona. Bounding the stationary distributions of the chemical master equation via mathematical programming. *J. Chem. Phys.*, 151(3):034109, 2019.

[22] E. Lakatos, A. Ale, P. D. W. Kirk, and M. P. H. Stumpf. Multivariate moment closure techniques for stochastic kinetic models. *J. Chem. Phys.*, 143(9):094107, 2015.

[23] A. Lamperski and S. Dhople. A semidefinite programming method for moment approximation in stochastic differential algebraic systems. In *IEEE Decis. Contr. P.*, pages 2455–2460, 2017.

[24] C. H. Lee. A moment closure method for stochastic chemical reaction networks with general kinetics. *MATCH - Commun. Math. Co.*, 70(3):785–800, 2013.

[25] Z. Li, X. Wang, and H. Zhang. Balancing the non-linear rosmarinic acid biosynthetic pathway by modular co-culture engineering. *Metab. Eng.*, 54:1–11, 2019.

[26] D. Liberzon. *Calculus of variations and optimal control theory.* Princeton university press, 2011.

[27] Y. T. Lin and C. R. Doering. Gene expression dynamics with stochastic bursts: Construction and exact results for a coarse-grained model. *Phys. Rev. E*, 93:022409, Feb 2016.

[28] D. Lunz. On continuum approximations of discrete-state markov processes of large system size. *Multiscale Model. Sim.*, 19(1):294–319, 2021.

[29] D. Lunz, G. Batt, J. Ruess, and J. F. Bonnans. Beyond the chemical master equation: Stochastic chemical kinetics coupled with auxiliary processes. *PLOS Comput. Biol.*, 17(7):1–24, 07 2021.

[30] D. Lunz and J. F. Bonnans. Optimal control of a two-species bioproducing microbial consortium. `https://hal.inria.fr/hal-03479385v2`.

[31] D. Lunz, J. F. Bonnans, and J. Ruess. Optimal control of bioproduction in the presence of population heterogeneity. `https://hal.inria.fr/hal-03445175`.

[32] D. L. Marchisio and R. O. Fox. Solution of population balance equations using the direct quadrature method of moments. *J. Aerosol Sci.*, 36(1):43–73, 2005.

[33] R. McGraw. Description of aerosol dynamics by the quadrature method of moments. *Aerosol Sci. Tech.*, 27(2):255–265, 1997.

[34] R. McGraw and D. L. Wright. Chemically resolved aerosol dynamics for internal mixtures by the quadrature method of moments. *J. Aerosol Sci.*, 34(2):189–209, 2003.

[35] P. Milner, C. S. Gillespie, and D. J. Wilkinson. Moment closure approximations for stochastic kinetic models with rational rate laws. *Math. Biosci.*, 231(2):99–104, 2011.

[36] B. Munsky, W. S. Hlavacek, and L. S. Tsimring. *Quantitative biology: theory, computational methods, and models.* MIT Press, 2018.

[37] I. Nåsell. An extension of the moment closure method. *Theor. Popul. Biol.*, 64(2):233–239, 2003.

[38] D. Nevozhay, R. M. Adams, E. Van Itallie, M. R. Bennett, and G. Balázsi. Mapping the environmental fitness landscape of a synthetic gene circuit. *PLOS Comput. Biol.*, 8(4):1–17, 04 2012.

[39] J. Paijmans, M. Bosman, P. R. ten Wolde, and D. K. Lubensky. Discrete gene replication events drive coupling between the cell cycle and circadian clocks. *P. Natl. Acad. Sci. USA*, 113(15):4063–4068, 2016.

[40] S. E. Pratsinis. Simultaneous nucleation, condensation, and coagulation in aerosol reactors. *J. Colloid Interf. Sci.*, 124(2):416–427, 1988.

[41] K. M. Rapp, J. P. Jenkins, and M. J. Betenbaugh. Partners for life: building microbial consortia for the future. *Curr. Opin. Biotech.*, 66:292–300, 2020.

[42] M. D. Rolfe, C. J. Rice, S. Lucchini, C. Pin, A. Thompson, A. D. S. Cameron, M. Alston, M. F. Stringer, R. P. Betts, J. Baranyi, M. W. Peck, and J. C. D. Hinton. Lag phase is a distinct growth phase that prepares bacteria for exponential growth and involves transient metal accumulation. *J. bacteriol.*, 194(3):686–701, 2012.

[43] D. Schnoerr, G. Sanguinetti, and R. Grima. Validity conditions for moment closure approximations in stochastic chemical kinetics. *J. Chem. Phys.*, 141(8):084103, 2014.

[44] D. Schnoerr, G. Sanguinetti, and R. Grima. Comparison of different moment-closure approximations for stochastic chemical kinetics. *J. Chem. Phys.*, 143(18):185101, 2015.

[45] D. Schnoerr, G. Sanguinetti, and R. Grima. Approximation and inference methods for stochastic biochemical kinetics—a tutorial review. *J. Phys. A - Math. Theor.*, 50(9):093001, jan 2017.

[46] L. F. Shampine and M. W. Reichelt. The matlab ode suite. *SIAM J. Sci. Comput.*, 18(1):1–22, 1997.

[47] A. Singh and J. P. Hespanha. Approximate moment dynamics for chemically reacting systems. *IEEE T. Automat. Cont.*, 56(2):414–418, 2011.

[48] P. Smadbeck and Y. N. Kaznessis. A closure scheme for chemical master equations. *P. Natl. Acad. Sci. USA*, 110(35):14261–14265, 2013.

[49] S. L. Spencer, S. Gaudet, J. G. Albeck, J. M. Burke, and P. K. Sorger. Non-genetic origins of cell-to-cell variability in trail-induced apoptosis. *Nature*, 459(7245):428–432, 2009.

[50] D. G. Spiller, C. D. Wood, D. A. Rand, and M. R. H. White. Measurement of single-cell dynamics. *Nature*, 465(7299):736–745, 2010.

[51] C. Tan, P. Marguet, and L. You. Emergent bistability by a growth-modulating positive feedback circuit. *Nat. Chem. Biol.*, 5(11):842–848, 2009.

[52] P. Thomas. Intrinsic and extrinsic noise of gene expression in lineage trees. *Sci. Rep.*, 9(1):1–16, 2019.

[53] L. N. Trefethen. *Approximation Theory and Approximation Practice*. SIAM, 2019.

[54] A. Wächter and L. T. Biegler. On the implementation of an interior-point filter line-search algorithm for large-scale nonlinear programming. *Math. Program.*, 106(1):25–57, March 2006.

[55] E. W. J. Wallace, D. T. Gillespie, K. R. Sanft, and L. R. Petzold. Linear noise approximation is valid over limited times for any chemical system that is sufficiently large. *IET Syst. Biol.*, 6(4):102–115, 2012.

[56] P. Whittle. On the use of the normal approximation in the treatment of stochastic processes. *J. Roy. Stat. Soc. B Met.*, 19(2):268–281, 1957.

[57] M. Yu, J. Lin, and T. Chan. A new moment method for solving the coagulation equation for particles in brownian motion. *Aerosol Sci. Tech.*, 42(9):705–713, 2008.

[58] K. Zhou, K. Qiao, S. Edgar, and G. Stephanopoulos. Distributing a metabolic pathway among a microbial consortium enhances production of natural products. *Nat. Biotechnol.*, 33(4):377–383, 2015.